Applied Mathematical Modelling 101 (2022) 694–715

Contents lists available at ScienceDirect

Applied Mathematical Modelling

journal homepage: www.elsevier.com/locate/apm

Neutron optics: New algorithm based on Green's functions for simulating waveguides with Dirichlet boundary conditions

I. Molina de la Peña[a,*], M.L. Calvo[a,*], R.F. Alvarez-Estrada[b]

[a] Departamento de Óptica, Facultad de Ciencias Físicas, Universidad Complutense, 28040 Madrid, Spain
[b] Departamento de Física Teórica, Facultad de Ciencias Físicas, Universidad Complutense, 28040 Madrid, Spain

ARTICLE INFO

Article history:
Received 13 December 2020
Revised 20 August 2021
Accepted 5 September 2021
Available online 15 September 2021

Keywords:
Neutron optics
Waveguides
Greenś functions
Dirichlet boundary conditions
Unbounded domain
Meshless algorithm

ABSTRACT

We present a new, efficient and robust method for computing scalar wave propagation for those cases in which Dirichlet boundary conditions play a key role. The algorithm is versatile and it allows to treat reflection, diffraction, waveguiding regime, scattering and free propagation. The analysis is based upon a representation for a slow neutron wavefunction in terms of the incoming wave and integrals, along the boundaries of an unbounded domain, involving a Green's function and certain auxiliary functions (warranting the Dirichlet boundary conditions). The analysis involves Fourier and Hilbert transforms defined only on the boundaries and enables to exploit the detailed advantages of Fast Fourier Transform (FFT) to perform simulations. Our algorithm proves to be highly effective both in terms in running time and memory load, compared to those based on Finite Differences Methods (FDM). Moreover, since the value of the field at each point may be calculated independently, this algorithm allows parallelization in a natural way.

1. Introduction

SubSection 1.1 summarizes a short introduction to the subject and, then, indicates how this work is organized. SubSection 1.2 outlines a useful previous analytical formulation.

1.1. Neutron optics

Neutron optics is the branch of neutron physics dealing with the theory and applications of the wave behaviour of slow neutrons. Being subatomic particles, neutrons propagation is governed by well-known Schrödinger's equation. If one assumes a t-independent potential for describing neutron interaction with the surrounding medium, the resulting equation for describing the steady state becomes:

$$\left[\frac{-\hbar^2}{2m}\nabla^2 + V(\boldsymbol{x}) - E\right]\varphi(\boldsymbol{x}) = 0 \tag{1}$$

* Corresponding authors.
E-mail addresses: imolinap@ucm.es (I. Molina de la Peña), mlcalvo@ucm.es (M.L. Calvo), rfa@ucm.es (R.F. Alvarez-Estrada).

https://doi.org/10.1016/j.apm.2021.09.007

$\varphi(\boldsymbol{x})$ is a steady wavefunction for describing a slow (thermal) neutron at the position $\boldsymbol{x}$, $\hbar$ is Planck's constant, m is the neutron mass, ∇^2 is the Laplacian, $E = \frac{2\pi^2\hbar^2}{m\lambda_{db}^2}$ is the neutron energy (the eigenvalue of the equation), λ_{db} is neutron's de Broglie wavelength and $V(\boldsymbol{x})$ is the scattering potential (due to strong nuclear forces) on the neutron at $\boldsymbol{x}$. The potential, in neutron optics in general, is the so called Fermi pseudopotential, $V = \frac{2\pi\hbar^2}{m} b\rho$, where ρ is the density of nuclei isotopes per unit volume and b is the bound scattering amplitude for a slow neutron scattered by a nucleus in the material. Since the material is assumed to be homogeneous, the potential does not depend on $\boldsymbol{x}$. Notice that $V(\boldsymbol{x}) = 0$ in vacuum. This is the choice in the present work.

In the physical situations treated here, the penetration of the slow neutron beam into the materials is not a large effect. Then, as a zeroth-order approximation, we shall neglect that penetration completely from the outset, as if the material would give rise to an infinite repulsive potential on the neutron. That approximation amounts to the Dirichlet Boundary condition. For a wider discussion, see [1].

Since mid70's to nowadays there have been several interesting theoretical proposals and experiments on neutron waveguides (those with small transverse cross section in comparison with standard ones [2,3]) in the framework of neutron optics. An earlier theoretical proposal came in 1973 for thin planar (2D) films by the use of selected materials with suitable refractive index (paying attention to Ti) [4]. On the other hand, similar theoretical proposals were made in 1984 and 1986 [5,6] for thin three-dimensional (3D) fibres.

First experimental demonstration came in 1994 by Feng et al. as they showed confined propagation of modes for slow neutrons in thin titanium films [7]. Since then, a number of significant works on confined slow neutron propagation in waveguides appeared (see [8-12]). In 1992, the focusing of slow neutrons by using polycapillary glass fibres was established [13,14].

Another important experiment in the context of neutron optics, but outside the waveguiding phenomenon, was performed by Kearney et al. [15], as they achieved the focusing of a slow neutron beam by neutron Fresnel lenses.

Those developments indicate the convenience of setting up and improving adequate mathematical and computational descriptions of slow neutron wave behaviour in neutron waveguides since relevant parameters as waveguide efficiency, critical angle and distribution of eigenmodes play a key role in these studies.

Here, we shall focus on the confined propagation of a beam of thermal neutrons (with $E = 0.025$ eV and λ_{db}=1.8 Å) in thin films or waveguides with transversal dimensions of the order of 100 nm and propagation lengths of the order of μm (longer propagation distances could also been considered). Therefore, such cases may be described, as a zeroth-order approximation, by means of the geometrical optics approximation, but, in so doing, most of the wave-like effects (i.e. the generation of propagations modes, diffraction effects, etc.…) would be lost. In our studies beam diffraction effects play a key role in the generation of propagation modes but, if one makes use of standard electromagnetic optics simulation algorithms, such as those based on Finite Differences Methods, FDM (for example FDTD, see [16,17]), then it would be necessary to simulate from about ten to twenty points per full wavelength (say a precision of 0.1 Å), for a correct performance.

In a previous paper [18], we stated that those simulations require a large amount of computation, both in memory load as well as in running time, then confronting a hard challenge to typical actual computers.

According to [19], the method presented in this paper could be regarded to fall on the category of a meshless, boundary-type method. There is an increasing demand of this kind of methods to deal with an enormous variety of systems, in many branches of research where FDM have been dominant.

We shall remind here two recent and interesting approaches. Firstly, generalized finite difference methods (GFDM) stand as relatively new and promising methods: in particular, the Peridynamic differential operator (PDDO) method constitutes a new type of GFDM which enjoys certain specific advantages. Specifically, PPDO is capable to reduce differentiation operators to suitable integrations, which facilitates the imposition of boundary conditions and the handling of sharp boundaries. See [19], where PDDO has been applied to Helmholtz-type acoustic problems in 2D. Secondly, we recall a recent improvement of the finite element method (FEM) to treat transient scalar wave propagation problems in unbounded domains [20]. Like in other FEM methods, the unbounded domain is replaced by a finite one by means of an artificial boundary: in [20] the improvement consists in prescribing certain absorbing (time-dependant) boundary condition. The latter is implemented through a suitable collocation approach (local in space and time). The performance of the method (which could be applied to waveguides) is tested numerically in several 2D examples.

We shall now summarize how the present work is organized. SubSection 1.2 reminds previous work for the wave equation inside a finite domain. The sections after subSection 1.2 report the present work devoted to the wave equation in an unbounded domain. Section 2 summarizes our generalization of subSection 1.2 (subSections 2.1 and 2.2.), the relation to Fourier transforms (subSection 2.3) and formulates our main development in this work, namely, the new algorithm (subSection 2.4). Section 3 is devoted to various applications of the algorithm and to the computational results. They are the following: Fourier transforms (FT) and Fast FT (FFT) for reconstruction (subSection 3.1), total reflection (subSection 3.2), aperture diffraction (subSection 3.3), different aspects of neutron waveguide (subSection 3.4), in particular, aperture diffraction with Sommerfeld-Rayleigh approximation, the corresponding computational results and geometrical interpretation and a video (subSections 3.4.1,3.4.2,3.4.3 and 3.4.4, respectively), Fresnel diffraction (subSection 3.5) and Arago-Poisson spot (subSection 3.6). Section 4 presents computational performance (subSection 4.1), discussions (subSection 4.2) and conclusions (subSection 4.3).

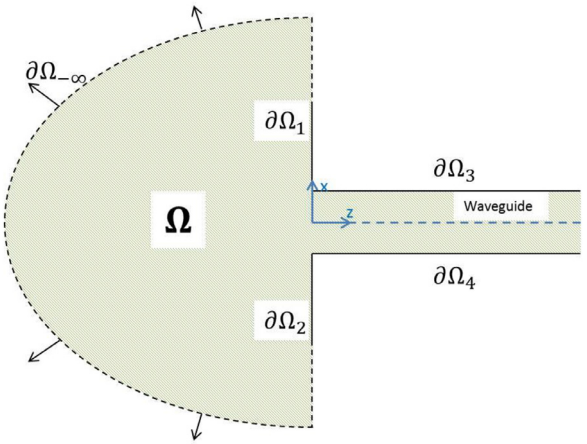

Fig. 1. Representation of the region of interest and its boundaries.

1.2. Previous analytical formulation

In 1970, Balian and Bloch analysed the eigenvalues of a wave equation associated to a large atomic nucleus [21]. In that paper, they studied the wave equation for a finite 3D (three-dimensional) domain bounded by a surface S, with Dirichlet, Neumann and mixed boundary conditions successively. They made use of a representation of the Green's function by means of the integral equation:

$$G(\boldsymbol{r}, \boldsymbol{r'}) = G_0(\boldsymbol{r}, \boldsymbol{r'}) + G_1(\boldsymbol{r}, \boldsymbol{r'}) \tag{2}$$

$$G_1(\boldsymbol{r}, \boldsymbol{r'}) = \int_S d\sigma_\alpha \frac{(\partial G_0(\boldsymbol{r}, \alpha))}{\partial \boldsymbol{n_\alpha}} \mu(\alpha, \boldsymbol{r'}) \tag{3}$$

Here, $G(\boldsymbol{r}, \boldsymbol{r'})$, $G_0(\boldsymbol{r},\boldsymbol{r'})$ and $G_1(\boldsymbol{r},\boldsymbol{r'})$ are the corresponding Green'functions for the finite domain, the infinite 3D space and the term arising from S, respectively. The differential with respect to $\boldsymbol{n_\alpha}$ represents the inner normal derivative at a generic point of the boundary surface S (namely, the scalar product of the gradient at a point times the inner unit vector normal to the surface at the same point). $d\sigma_\alpha$ is the differential element. The integration is performed over S and $\mu(\alpha, \boldsymbol{r'})$ is an auxiliary function to be determined when imposing the boundary condition.

Notice that $G_1(\boldsymbol{r},\boldsymbol{r'})$ in Eq. (3) is formulated for the Dirichlet boundary condition and it is interpreted as a "*double layer potential*".

Moreover, Balian and Bloch [21] have derived certain fundamental relations between the auxiliary functions, $\mu(\alpha, \boldsymbol{r'})$ and the Green's function $G_0(\boldsymbol{r},\boldsymbol{r'})$, in order to obey the boundary conditions. Those results led them to propose iterative algorithms for numerically approximating Eq. (2) under Dirichlet boundary conditions (enabling them to extend the algorithms to other boundary conditions). Those algorithms were based upon Green's function, $G_1(\boldsymbol{r},\boldsymbol{r'})$ and iterations at each step (for more details see [21]).

In our approach, we make use of a representation for the slow neutron wavefunction, $\varphi(\boldsymbol{x})$, by extending Eq. (2) and, by replacing, in it, the inhomogeneous term $G_0(\boldsymbol{r},\boldsymbol{r'})$ by another one, $\varphi_{in}(\boldsymbol{x})$, representing the incoming neutron wave. At a later stage, we shall develop a different approach. We shall set our algorithm to update the value of the corresponding auxiliary functions, $\mu_i(\boldsymbol{x_i})$, in Eq. (5), as we shall explain.

2. Theory and calculation

In our previous paper [1], we developed an analysis of the behaviour of a thermal neutron beam in an unbounded 2D (two-dimensional) ideal waveguide (thin film) under the assumption of Dirichlet boundary conditions. In that case, we set the potential to be: i) that of vacuum, $V(\boldsymbol{x}) = 0$, inside the waveguide and outside it and ii) $V(\boldsymbol{x}) = +\infty$ in the clad (i.e., the outer region limiting the waveguide), that is, the repulsive potential of the clad is approximated by an infinitely repulsive one.

In the actual case, Eq. (1) reduces, in our region of interest (inside the waveguide and outside it), to a homogeneous Helmholtz equation for the slow neutron wavefunction, $\varphi(\boldsymbol{x})$:

$$\left[\nabla^2 + K_{in}^2\right]\varphi(\boldsymbol{x}) = 0 \tag{4}$$

where $K_{in}^2 = 2mE/\hbar^2$ is the squared wavevector associated to the incoming slow neutron far from the waveguide.

Our domain of analysis was then limited to a semiinfinite 2D waveguide as in Fig. 1, in which four walls are limiting the waveguide entrance ($\partial\Omega_{1,2}$) and the waveguide clad ($\partial\Omega_{3,4}$), respectively. The clad is the set of two infinite 2D domains

(specifically, two quadrants) into which the slow neutron cannot penetrate (so that $\lim_{\boldsymbol{x}\to\partial\Omega_{1...4}}\varphi(\boldsymbol{x})=0$, as the clad is approached from outside it). The domain Ω was the infinite 2D domain into which the neutron can propagate, including the interior of the waveguide (with non-vanishing $\varphi(\boldsymbol{x})$). The domain is limited by $\partial\Omega_i (i=1,2,3,4)$ as seen in Fig. 1.

Since our main interest is the characterization of neutron waveguides, we focused our attention to this geometry. Anyway, this formulation may be extended to an arbitrary number, n, of subdivisions for the boundaries to solve any other geometry that obeys Dirichlet boundary conditions.

2.1. Inhomogeneous term and integral representation for the neutron wavefunction

To obtain a representation of the slow neutron wavefunction $\varphi(\boldsymbol{x})$ in terms of Green's function, we will extend the formalism of Balian and Bloch [21], displayed in Eqs. (2) and (3).

While Balian and Bloch considered a finite region of 3D space (i.e., the atomic nucleus), we shall deal with geometries in infinite or unbounded space (see Fig. 1, in that case and for convenience, a semiinfinite 2D waveguide) that lead to the nontrivial inclusion of an inhomogeneous term $\varphi_{in}(\boldsymbol{x})$ representing the incoming slow neutron wave (instead of $G_0(\boldsymbol{r},\boldsymbol{r}')$ in Eq. (2)). This $\varphi_{in}(\boldsymbol{x})$ comes from the need of closing the integrating region Ω at $-\infty$. An inspection to Fig. 1 shows that Dirichlet conditions are obeyed on the boundaries $\partial\Omega_i$, $i=1...4$ but not when closing the boundary at $-\infty$ (i.e. $\partial\Omega_{-\infty}$).

Greenś theorem [22-24] ensures that this term $\varphi_{in}(\boldsymbol{x})$ corresponds to the incident wave. For previous approaches to the structures in Eqs. (2) and (3) with the corresponding inhomogeneous terms (based upon electrostatics equations like the Laplace one) see Ref. [25].

Regarding the geometry stated in Fig. 1, one has the following representation for the slow neutron wavefunction $\varphi(\boldsymbol{x})$ that solves Eq. (4) with Dirichlet boundary conditions ($\boldsymbol{x}$ being a 2D vector):

$$\varphi(\boldsymbol{x})=\varphi_{in}(\boldsymbol{x})+\sum_{i=1}^{4}\int_{\partial\Omega_i}d\Omega_i\,\frac{\partial G(\boldsymbol{x}-\boldsymbol{x'_i})}{\partial\boldsymbol{n_i}}\bigg|_{\boldsymbol{x'_i}\,\in\,\partial\Omega_i}\mu_i(\boldsymbol{x'_i}) \tag{5}$$

Here, $\varphi_{in}(\boldsymbol{x})=e^{i\boldsymbol{K_{in}}\cdot\boldsymbol{x}}$ corresponds to an incident free plane wave with wavevector $\boldsymbol{K_{in}}$ (solving Eq. (4)), $\partial\Omega_i$ corresponds to each of the four Dirichlet line boundaries (see Fig. 1), $\partial/\partial\boldsymbol{n_i}$ represents the normal derivative to the corresponding boundary line [1]. $\mu_i(\boldsymbol{x'_i})$ is an auxiliary function defined in the boundary, interpreted as the density for a double layer potential. $G(\boldsymbol{x}-\boldsymbol{x'_i})$ is 2D Green's function (the counterpart of $G_0(\boldsymbol{r},\boldsymbol{r'})$ in [21] see Eq. (2)) determined by the set of all plane waves in the infinite 2D space:

$$G(\boldsymbol{x}-\boldsymbol{x'})=-\iint_{-\infty}^{\infty}\frac{d^2\boldsymbol{K'}}{(2\pi)^2}\,\frac{exp[i\boldsymbol{K'}(\boldsymbol{x}-\boldsymbol{x'})]}{E+i\varepsilon-\frac{\hbar^2}{2m}\boldsymbol{K'^2}} \tag{6}$$

where $E=\frac{\hbar^2\boldsymbol{K_{in}^2}}{2m}$ is the total energy of the incident wave ($\boldsymbol{K_{in}^2}$ being the squared modulus of a 2D wavevector).

Notice that $\varepsilon>0$ is an infinitesimal term and that the limit $\varepsilon\to 0$ is taken at the end of the calculations. A detailed and rigorous derivation of the general solution of Laplaceś equation inside a finite volume with Dirichlet (and Neumann) boundary conditions is given in [25]. That derivation, omitted here for brevity, can be readily extended to Eq. (4) and yields Eq. (5), as it happened with Eqs. (2) and (3).

Notice that integrals, containing the Greenś function in Eq. (6), contribute in the right-hand-side of Eq. (5). Those Greenś functions are locally singular, but the integrals containing them in Eq. (5) are finite, as shown in [1] that is, the local singularities are smoothed out by the integration.

It is trivial to show that all terms in the right-hand-side of Eq. (5) fulfil Eq. (4), since so does $\varphi_{in}(\boldsymbol{x})$ and each integral (due to the Greenś function inside it) also satisfies Eq. (4) for any $\mu_i(x'_i)$. The problem is now to determine the functions $\mu_i(x'_i)$ that fulfil the Dirichlet conditions.

2.2. Dirichlet boundary conditions

Here, we shall ensure that the density functions $\mu_i(x'_i)$ fulfil the Dirichlet conditions. Balian and Bloch [21] derived such conditions stating that $G(\boldsymbol{r},\boldsymbol{r'})$: i) must be continuous inside the volume bounded by the surface S and vanish as the vector $\boldsymbol{r}$ approaches the boundary from inside S, ii) does not vanish at the boundaries (that is, if $\boldsymbol{r}$ is taken to lie exactly at the boundaries, without the process of approaching them from inside) . The extension of i) and ii) to Eq. (5) (to obtain conditions for $\mu_i(x'_i)$) reads:

$$\lim_{\boldsymbol{x}\to\partial\Omega}\varphi(\boldsymbol{x})=0 \tag{7}$$

as $\boldsymbol{x}$ approaches a point x'_i in each boundary line from outside the clad (see Fig. 1), while ii) at x'_i, $\varphi(x'_i)$ is different from 0.

In our previous paper [1], we performed the detailed derivation considering the actual inhomogeneous term and the set of Dirichlet boundaries (i.e. semiinfinite waveguide entrance and walls in Fig. 1). We get, for $i=1,2,3,4$:

$$\frac{1}{2}\frac{2m}{\hbar^2}\mu_i(x'_i)=-\varphi_{in}(x'_i)-\sum_{\substack{i=1\\ j\neq i}}^{4}\int_{\partial\Omega_j}d\Omega_j\,\frac{\partial G(x_i-x'_j)}{\partial n_j}\bigg|_{x'_j\,\in\,\partial\Omega_j}\mu_j(x'_j) \tag{8}$$

We obtain, in this way, a system of four inhomogeneous linear integral equations for $\mu_i = f(\mu_j,\mu_k,\mu_l)$; $i \neq j, k, l$.
By comparing Eq. (8) with Eq. (5), we get:

$$\frac{1}{2}\frac{2m}{\hbar^2}\mu_i(x_i') = -\varphi(x_i') \tag{9}$$

Eq. (9) shows that, in order to fulfil the Dirichlet boundary conditions, the functions $\mu_i(x_i')$ must be proportional to the wavefunction at the same point in the corresponding boundary line. This seems physically acceptable and quite useful upon proceeding to the extinction theorem [1]. The treatment allows a generalization to any arbitrary set of Dirichlet boundary lines in the region Ω as well as extending it to 3D geometries.

2.3. Relation to Fourier Transform representation

Once characterized the auxiliary functions, $\mu_i(x_i')$, one has to implement them in the wavefunction equation, Eq. (5). We shall now show an example for a particular boundary line in Fig. 1 in 2D, $\boldsymbol{x} = (x, z)$ (its generalization to 3D being straight).

Consider the upper boundary line of the waveguide, $\partial\Omega_3$ as $x = +x_0/2$, $z \geq 0$ (where the parameter x_0 is the waveguide aperture). We assume an incoming neutron wave with a well-defined wavevector (with $\boldsymbol{K_{in}^2} = 2mE/\hbar^2$).

The associated auxiliary function $\mu_3(z)$ for this boundary line is given through Eq. (9). One may introduce it in Eq. (5), together with the Green's function in Eq. (6), and perform some direct operations. In this case, the term associated to $\mu_3(z)$ turns out to be (for details, see [1]):

$$\Lambda_3(x,z) = \int \frac{dK'_z}{2\pi}\left[\int_0^\infty dz'\varphi\left(\frac{x_0}{2},z'\right)e^{-iK'_z z'}\right]e^{iK'_z z}e^{-i\left(x-\frac{x_0}{2}\right)\sqrt{\frac{2mE}{\hbar^2}-K_z'^2}} \tag{10}$$

The integral in Eq. (10) can be interpreted as the Fourier transform of the function $H(z')\varphi(x = x_0/2, z')$ where $H(z')$ is the Heaviside step function:

$$\Lambda_3(x,z) = \int \frac{dK'_z}{2\pi}F\left[H(z')\varphi\left(\frac{x_0}{2},z'\right)\right]e^{iK'_z z}e^{-i\left(x-\frac{x_0}{2}\right)\sqrt{\frac{2mE}{\hbar^2}-K_z'^2}} \tag{11}$$

Here F denotes the Fourier transform operator acting on the inner function. A deeper look at Eq. (11) shows that, again, one has to compute the inverse Fourier transform from the previous one, taking into account the correction that comes from the limits of the boundaries (i.e., the Heaviside step function). In [1] we related this operation to the Hilbert transform in our formulation (as it could be expected from signal theory analysis). It can be seen that this term (i.e. arising from the waveguide's entrance) gives rise to aperture diffraction.

The other terms of Eq. (5) are obtained in the same way and they relate to the Fourier transform of the wavefunction in the boundaries ($\varphi(\partial\Omega_i)$) as in Eq. (9), modulated by the geometrical limits of the boundary (i.e., the use of Heaviside step function).

Our algorithm here is based upon Eqs. (8) and (9). Again, Eq. (8) has, in its right-hand-side, integrals containing those locally singular Greenś functions. However, the integrals in Eq. (8) can also be shown to be convergent [1]. Our algorithm is formulated so as neither to meet nor be disturbed by those local singularities anywhere.

2.4. Formulation and implementation of a new practical algorithm

In this subsection we present a numerical iterative algorithm for the simulation of those situations, which may be described by an incoming wave and a number of boundaries involving Dirichlet conditions. Our algorithm is inspired by the interpretation (Balian and Bloch [21]) of the correction to the Green's function, $G_1(\boldsymbol{r},\boldsymbol{r'})$, as a multiple reflection. We will analyse this aspect later, in Section 3.4.3.

In our case, our interest is to simulate a semiinfinite waveguide from $z = 0$ to $z = +\infty$ as presented in Fig. 1. As it will be seen in Section 3, it is trivial to compute other cases using this formulation (free propagation field, aperture diffraction, total reflection, waveguiding…) while geometry obeys Dirichlet boundary conditions.

Summarizing, we shall obtain $\varphi(\boldsymbol{x})$ in Eq. (5) by using the Green's function in Eq. (6), the system of four equations for $\mu_i(x_i')$ in Eq. (9) and the interpretation of the terms that will arise, as the result of the Fourier transform of the wavefunction propagating along the boundaries.

Our algorithm has various sequential steps, to be performed for any angle of incidence of the incoming wave (see Fig. 2):

1- Compute the values of the incident wave, $\varphi_{in}(\boldsymbol{x})$ both in each point of the defined mesh, Ω and in each point of the defined boundaries, $\partial\Omega_i$, $i = 1…n$.
2- Use the values of $\varphi_{in}(\boldsymbol{x})$ computed over the boundaries in step 1, where Dirichlet conditions are imposed, to calculate the corresponding auxiliary functions, μ_i. Initially, the complex value for each point of the auxiliary functions, μ_i, is proportional to the value of the incident wave, φ_{in} at the same point by applying Eq. (9): $\mu_i(\boldsymbol{x'_i}) = -\frac{\hbar^2}{m}\varphi_{in}(\boldsymbol{x'_i})$, where $\boldsymbol{x'_i}$ is the set of points of the boundary $\partial\Omega_i$ where Dirichlet conditions are imposed.

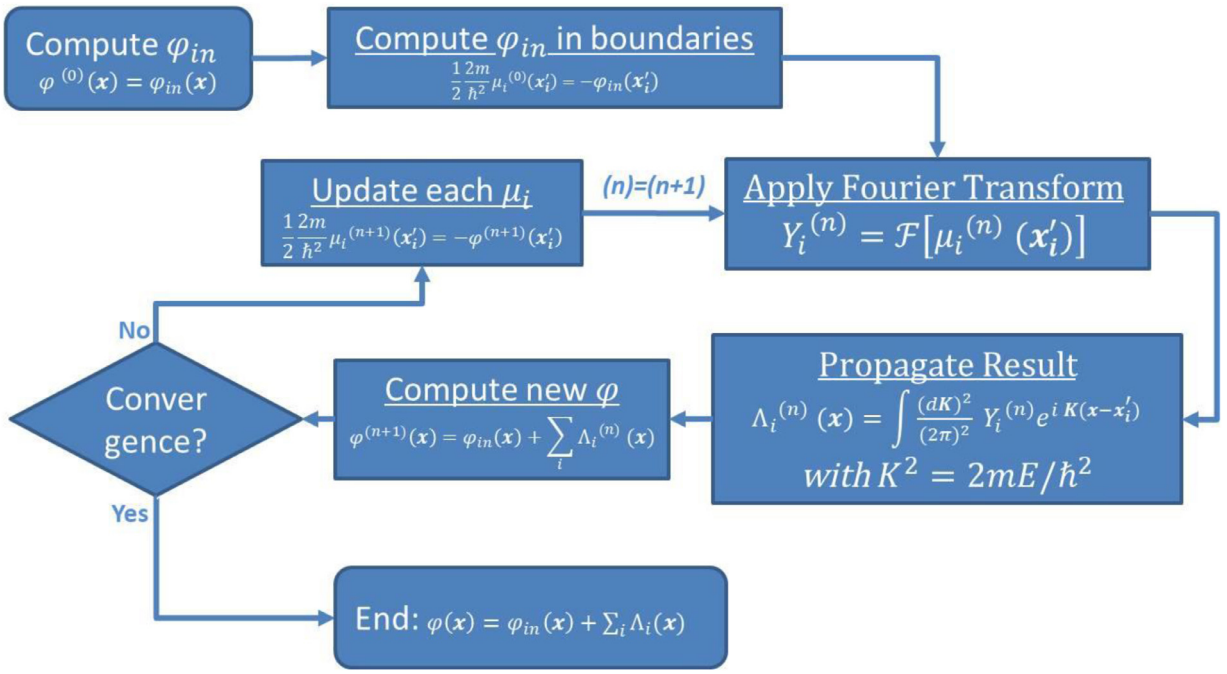

Fig. 2. Algorithm flux diagram.

3- Perform the Fourier transform of each function, μ_i calculated in each boundary: $Y_i^{(n)}(\boldsymbol{K'}) = \mathcal{F}[\mu_i^{(n)}(\boldsymbol{x'_i})](\boldsymbol{K'})$, where (n) stands for the number of the iteration. This step only relates to calculate the auxiliary functions in the wavevector (spatial frequency) domain. Notice that, since our method comes from the context of neutron optics, the wavector relates with the neutron energy, $\boldsymbol{K}'^2 = 2mE/\hbar^2$.

4- Propagate and integrate the obtained result, for each boundary, $\partial\Omega_i$, according to Eq. (11) (or similar ones, depending on the geometry). Thus, the function propagated from the boundary, $\partial\Omega_i$, to the point $\boldsymbol{x}$ is $\Lambda_i(\boldsymbol{x}) = \int \frac{d\boldsymbol{K'}}{(2\pi)^2} Y_i^{(n)}(\boldsymbol{K'}) e^{i\mathbf{K'}(\mathbf{x}-\mathbf{x'_i})}$. Notice that wavevector $\boldsymbol{K'}$ has one dimension less than vector $\boldsymbol{x}$ since it arises from the Fourier transform of the auxiliary function, $\mu_i(\boldsymbol{x'_i})$, that is constrained to the boundary $\partial\Omega_i$. Consequently, wavector $\boldsymbol{K'}$ must obey that $\boldsymbol{K'}^2 = 2mE/\hbar^2$. This condition is set by the chosen boundary geometry. For example, in Eq. (11), as the boundary $\partial\Omega_3$ is $x = +x_0/2$, $z \geq 0$, it implies that $\boldsymbol{K'}(\boldsymbol{x} - \boldsymbol{x'_i}) = K'_z z - (x - \frac{x_0}{2})\sqrt{\frac{2mE}{\hbar^2} - K_z'^2}$

5- Compute a new updated solution for the wavefunction by adding the functions propagated from each boundary, $\partial\Omega_i$, with the incident wave, according to Eq. (5): $\varphi(\boldsymbol{x}) = \varphi_{in}(\boldsymbol{x}) + \sum_i \Lambda_i(\boldsymbol{x})$

6- Compute a new updated function μ_i for each boundary applying Eq. (9), using the result in step 5.

7- Iterate the above steps 3 to 6, until convergence is achieved. The latter occurs, naturally, when the change in each μ_i is smaller than a chosen value. Moreover, one may impose any other convergence condition (for example, a total flux value through an aperture).

Fig. 2 summarizes and displays this algorithm

Notice that: a) Step 3 can be easily computed making use of Fast Fourier Transform [26] algorithms available in any commercial mathematical package. Nevertheless, we do not choose any a priori method (for example, the use of numerical integration, any other Discrete Fourier Transform…) b) our algorithm reduces the amount of running time in comparison to others, since the former only deals with the wavefunction values on the boundaries, instead of in the whole volume, and c) as it can be seen in Eq. (5), once the auxiliary functions, μ_i are known, the computation at each point is carried out independently, then, parallelization is trivial and, moreover, one can focus on a limited region instead of having to deal with the whole volume.

As stated in the introduction, this method relates to that of PDDO presented in [19,20], being a meshless, boundary-type method. PDDO method in [19,20] makes use of the so called peridynamic function to obtain, via integration of values of a boundary, the values of any order derivative in any region in the space. These functions are smooth and well-conditioned, instead of Greenś functions that have singularities that must be treated analytically. In the present paper, although we do employ Greenś functions, their singularities do not affect our numerical algorithm in any way since we can perform direct computation without additional manipulations.

In comparison, our method in [1], using Green's function, relates only with the wave equation. Notice, in most methods one must set an artificial reflectionless finite boundary for simulating unbounded domains. With the present method, this becomes trivial, since Sommerfeld radiation condition is already carried by the Green's function and, so, it is only needed not to define nor compute an auxiliary function, μ_i.

3. Results

We shall show simulations for different cases as well as the runtime durations required for them. Our simulations for subSections 3.2 to 3.4 are performed in 2D space and subSections 3.5 and 3.6 are performed in 3D space. In principle, Eq. (4) is formulated in 3D Cartesian coordinates $\boldsymbol{x} = (x, y, z)$. Since each dimension x, y, z may play an independent role, one may restrict to 2D space, provided that one restricts the incoming wavevector, $\boldsymbol{K}^2 = 2mE/\hbar^2$; $\boldsymbol{K} = (K_x,K_y,K_z)$ to $K_y = 0$. Then, we will consider only the (x, z) coordinates, assuming that the waveguide is infinite in y direction (i.e., we simulate neutron thin films). Anyway, our results in 2D can be readily extended if one adds the missing (y) coordinate and K_y component of the wavevector.

3.1. Use of numerical Fourier Transform or inverse Fast Fourier Transform for field reconstruction

As stated in subSection 2.4, the algorithm requires the use of Fourier transforms. In this section we discuss different methods for computing these transforms.

FFT algorithm, any other DFT algorithm or even numerical or analytical integration may be used. Fast Fourier Transform (FFT) [26] has well known advantages: running time (since it scales as $O(nLog(n))$ [27]), simplicity of implementation and accessibility and readiness to be used in many commercial packages.

We have used FFT algorithm in Step 3, in all our simulations, (recall subSection 2.4), but in Step 4 we have implemented two approaches depending on the case. In one approach, we implement the direct formulation as in Eq. (11) for propagating the Fourier transform through numerical integration. In the second approach we interpret the terms in Eq. (11) as an inverse Fourier transform in z coordinate modulated by a phase factor depending on x. This may be computed by using the inverse for the FFT algorithm (IFFT). One disadvantage is that, using both FFT and IFFT, wavefunction points are not calculated independently and, so, parallel calculations may not be performed. If, once computed with some resolution, one wants to focus on any region (as we do in Fig. 5b), the entire region Ω must be computed with a different grid resolution from scratch. On the other hand, this procedure is several times faster that performing a numerical integration.

Certainly, there are other options for computing both Fourier and inverse Fourier transforms (with features such as a better control of frequencies, signal filtering, etc.…) but we chose a general method.

When representing in figures the results for different cases, we indicate the method used for propagating the Fourier transform.

3.2. Particular case: total reflection for slow neutron beam free propagation

Total reflection for slow neutron beam free propagation, here simulated, is the simplest case to be considered for this algorithm. In fact, it can be solved analytically by making use of Eqs. (5) and (6) and imposing as auxiliary function: $\frac{1}{2}\frac{2m}{\hbar^2}\mu(x) = -\varphi_{in}(x, z = 0) = -e^{iK_x x}$.

Let us suppose that the domain, Ω, is an empty medium (vacuum) for negative z (i.e., $-\infty < z \leq 0$, $\forall x$) and that for positive z and any x there is an infinitely repulsive potential barrier. Consider a monochromatic neutron plane wave, impinging the barrier with an arbitrary angle of incidence: $\varphi_{in}(x, z) = exp(iK_x x + iK_z z)$ with total energy $E = 0.025\ eV$ ($\lambda_{db} = 1.8$ Å) and squared wavevector $K_x^2 + K_z^2 = 2mE/\hbar^2$. In order to simplify, we shall represent the neutron beam by the previous plane wave apodized by a window function:

$$\varphi_{in}(x, z) = rect\left(\frac{x - \frac{K_x}{K_z}z}{1000}\right)e^{iK_x x}e^{iK_z z} \tag{12}$$

where *rect* is the window function. We choose the parameters so as to have a 1000 Å centred geometric shadow in the barrier.

As it can be seen in Table 1a for cases "15° reflection" and "30° reflection", the use of the algorithm is straight. In this case, only one auxiliary function $\mu_1(x)$ is defined from the value of the impinging incoming wave $\varphi_{in}(x, z = 0)$ and, moreover, only one iteration is needed to compute the final result (i.e.: the auxiliary function is not updated), since the reflected wave will travel towards $z \to -\infty$ and, consequently, the value of the auxiliary function in the boundary will remain unchanged.

The results are displayed in Figs. 3a and 3b, respectively. These figures, display the squared modulus of the neutron wavefunction which is represented by means of different colours at each point (x, y). Right colourbar represents the correspondence between values and colour, assuming the square modulus of φ_{in} to be 1. We notice the following features: a) the incoming wave and its geometrical reflection, with the same incidence angle, b) the diffraction pattern produced by the outgoing wave, due to the window function, behaving similarly to a finite aperture, and c) the interaction fringes formed in

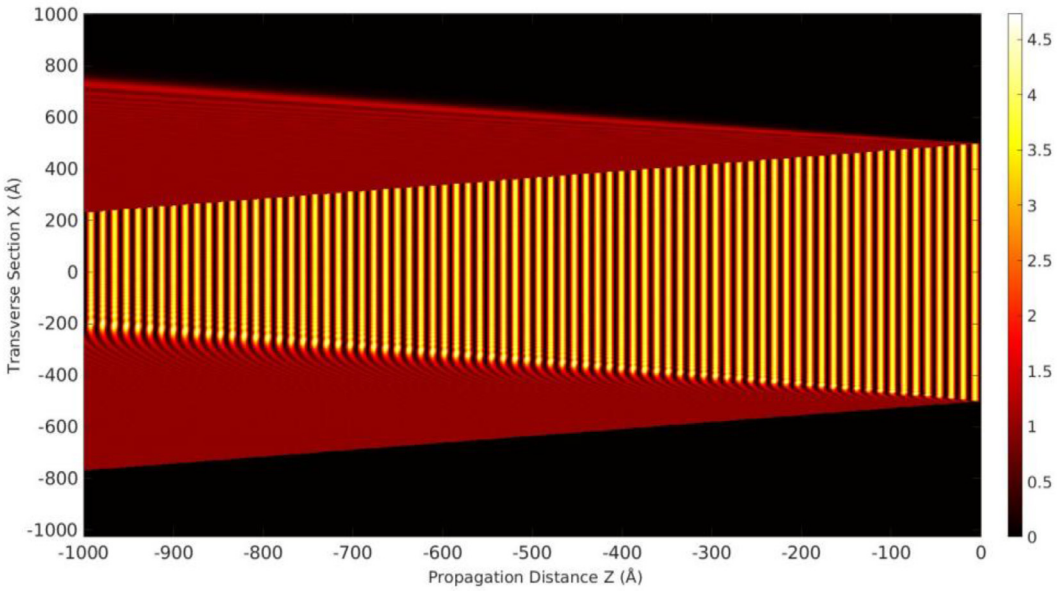

a) Case for 15º. $E = 0.025eV$ ($\lambda_{db} = 1.8$ Å)

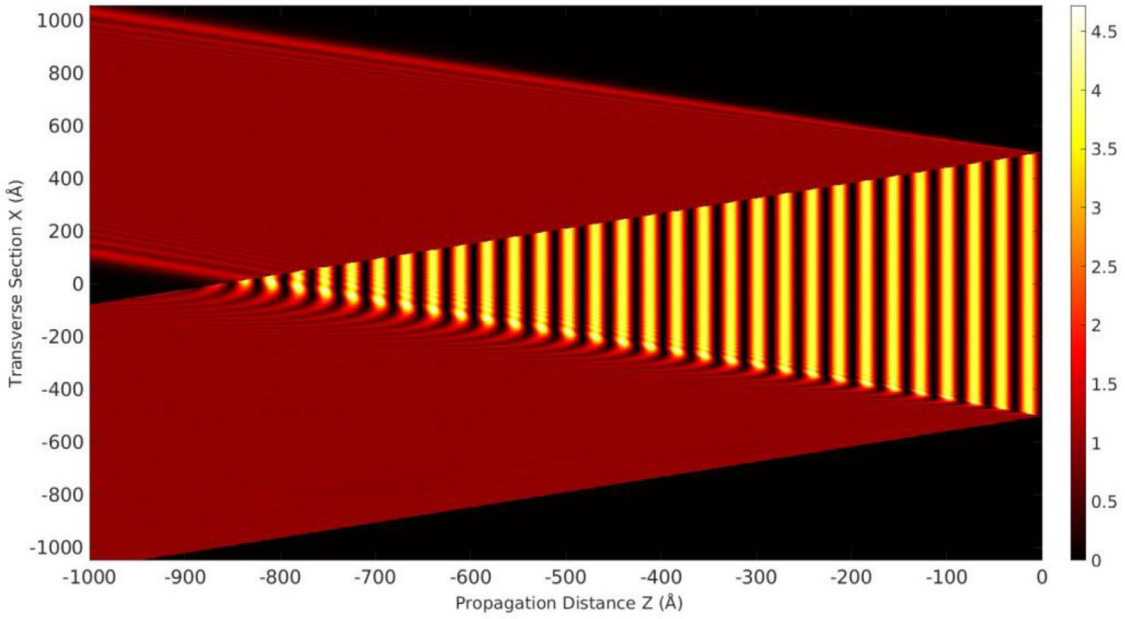

b) Case for 30º, $E = 0.025eV$ ($\lambda_{db} = 1.8$ Å).

Fig. 3. Simulation of the backward reflection of a neutron plane wave beam (see Table 1a and 1b). a) Case for 15°. $E = 0.025$ eV ($\lambda_{db} = 1.8$ Å) b) Case for 30°, E= 0.025 eV ($\lambda_{db} = 1.8$ Å).

the superposition zone where the incoming and outgoing waves overlap. Notice that there is a spurious Moire effect due to the resolution of the image generated by MATLAB and the frequencies of the represented waves (the order of 1.8 Å). This effect may be corrected by adding more resolution to the image but then it requires more computing time and memory consumption.

3.3. Case: slow neutron beam diffraction by a limited aperture

A key phenomenon, both for quantum and electromagnetic wave equations, is the diffraction produced by a single slit and, so, we make use of a free-propagating aperture diffraction phenomenon for checking the algorithm well-performance.

Let us suppose that the positive z region (i.e. $0 \leq z < \infty$, $\forall x$), is now an empty medium (vacuum). Located at $z = 0$, $-\infty < x < \infty$ there is a very thin screen with an aperture of size 1000 Å centred at the origin. From $z \to -\infty$, an incoming monochromatic neutron plane wave with arbitrary incidence angle and total energy $E = 0.025\ eV$ ($(\lambda_{db} = 1.8$ Å$)$) impinges the screen. Because of this interaction, we set Dirichlet boundary conditions at the screen but not on the aperture and perform a free propagation of the resulting wave in the region $0 \leq z < +\infty$, $\forall x$. The expected result may show the corresponding diffraction pattern.

In this case, as it can be seen in Table 1a for cases "0° aperture diffraction" and "10° aperture diffraction", we introduce two auxiliary functions. The Dirichlet condition leads to the actual counterpart of Eq. (9). Then, the auxiliary functions turn out to be proportional to the incoming wavefunction in the boundary; i.e.:$\mu_1(x) = -\hbar^2/m\varphi_{in}(x,\ z = 0) \forall x \geq +x_0/2$ and $\mu_2(x) = -\hbar^2/m\varphi_{in}(x,\ z = 0) \forall x \leq -x_0/2$ (where x_0 is the size of the aperture). The total result corresponds to the incoming wave minus the propagation of these two terms (as in step 7, see Fig. 2). This could be interpreted as performing numerically the extinction theorem at the screen. As shown in Table 1b, one iteration is required, as in the previous case, since the free propagating wave propagates for $z \to +\infty$ and thus, the auxiliary functions do not need to be updated.

Figs. 4a and 4b show the numerical results for the aperture diffraction for an incoming wave of 0° and 10° of angle of incidence. These figures display the squared modulus of the neutron wavefunction which is represented by means of different colours at each point $(x,\ z)$. We observe the expected results since: a) a slight diffraction pattern appears as the wave propagates in space, b) the main propagation angle is maintained.

Notice the resolution of this algorithm: it is efficient in scales involving a wavelength $\lambda_{db} = 1.8$ Å, apertures of 10^3 Å and propagations of 10^3 Å. These simulations would require a high consumption in memory and/or computation, if they would be performed using finite differences methods.

3.4. Case: neutron waveguide

We will concentrate in neutron waveguides as a case other than free propagation. Thus, we will check the validity of the algorithm for this phenomenon.

By inspecting Figs. 3 and 4 above, we state that confinement could be described, as a first approximation, by means of classical (geometrical) optics. These scales will not produce a strong diffraction pattern.

The wave behaviour, even if a small (or non-dominant) effect, cannot be neglected, in particular if one wants to characterize the propagation modes generated in waveguides.

In the present case, we set our domain of interest, Ω, as a semiinfinite waveguiding thin film, thereby continuing to focus on the XZ plane by means of a 2D formulation, as seen in Table 1a for "waveguide" case, centred at the origin of coordinates and parallel to z axis from $z = 0$ to $z \to \infty$. Thus, the waveguide is limited by four walls (defining the clad), located at; $(x \geq +x_0/2,\ z = 0)$, $(x \leq -x_0/2,\ z = 0)$, $(x = +x_0/2,\ z \geq 0)$ and $(x = -x_0/2,\ z \geq 0)$, where x_0 is the waveguide aperture. See Fig. 1, in which the right region represents the waveguide.

We remind here that in the four walls of the waveguide defining the boundaries (where we impose Dirichlet conditions, using Eq. (9)), we define four auxiliary functions, one for each wall; $\mu_1(x) = -\hbar^2/m\varphi(x,\ z = 0)$ for $\infty > x \geq x_0/2$; $\mu_2(x) = -\hbar^2/m\varphi(x,\ z = 0)$ for $-x_0/2 \geq x > -\infty$; $\mu_3(z) = -\hbar^2/m\varphi(x = x_0/2,\ z)$ for $z \geq 0$ and $\mu_4(z) = -\hbar^2/m\varphi(x = -x_0/2,\ z)$ for $z \geq 0$. The iterative updating of these four functions by using recursively Eq. (9) will lead to our numerical solution.

In a previous study of such waveguides in [1], we considered two main effects: a) the waveguide's aperture diffraction effects, and b) the generation of propagation modes. Even if both effects cannot be strictly separated from each other, one can state approximately that the first one (a) is related to the auxiliary functions $\mu_1(x)$ and $\mu_2(x)$ and that the second one (b) to $\mu_3(z)$ and $\mu_4(z)$, respectively. Thus, as a first approximation, one can separate these two effects in the simulations.

First, we compute $\mu_1(x)$ and $\mu_2(x)$ (similarly to the case of the aperture diffraction in Section 3.3). Then, we use this result as an incoming (diffracted) wave for propagating into the waveguide with $\mu_3(z)$ and $\mu_4(z)$, that take part into confinement effects (see subsection3.4.3). With this approach, $\mu_1(x)$ and $\mu_2(x)$ are not updated and we only update recursively $\mu_3(z)$ and $\mu_4(z)$. With this strategy we get a better control of the simulations.

3.4.1. Approximation through the 2D-Sommerfeld-Rayleigh integral representation

In order to approximate the diffraction effects of the aperture of the waveguide, we shall use a new $\varphi^*_{in}(x, z)$ (will replace and approximate the former incoming plane wave $\varphi_{in}(x,\ z)$ and the auxiliary functions $\mu_1(x)$ and $\mu_2(x)$). This will enable us afterwards to concentrate on $\mu_3(z)$ and $\mu_4(z)$.

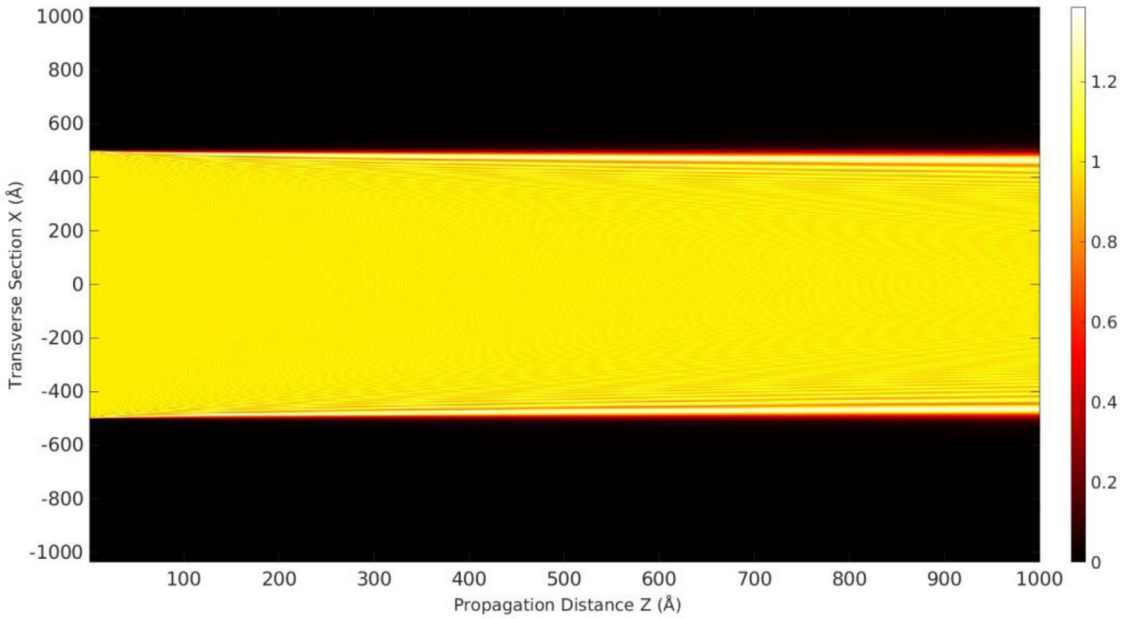

a) Case for 0º $E = 0.025eV$ ($\lambda_{db} = 1.8$ Å)

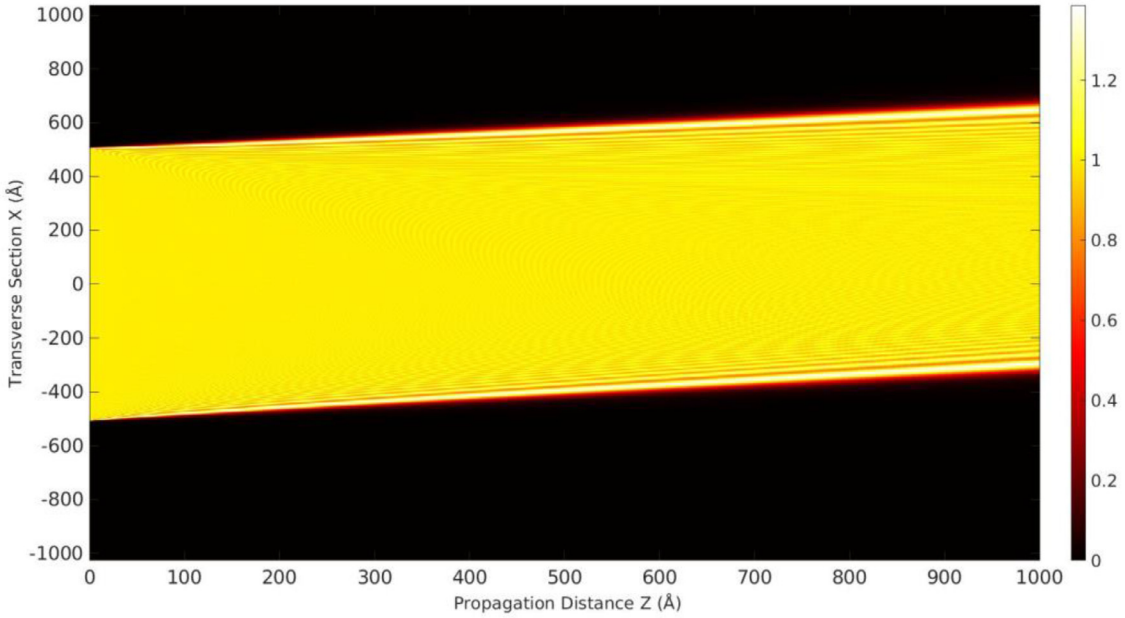

b) Case for 10º $E = 0.025eV$ ($\lambda_{db} = 1.8$ Å)

Fig. 4. Diffraction of a neutron plane wave by a 1000 Å aperture. a) Case for 0° $E = 0.025$ eV ($\lambda_{db} = 1.8$ Å) b) Case for 10° $E = 0.025$ eV ($\lambda_{db} = 1.8$ Å).

Here, we shall remind the Sommerfeld-Rayleigh integrals (see refs[22-24]. and [28]) for a screen with a limited aperture. This approach will provide us a direct procedure to save computing memory.

In our case, the 2D Green's function in Eq. (6) [24] is considered in the Sommerfeld-Rayleigh integral below. Then Eq. (6) is:

$$G(r) = \frac{i}{4} H_0^{(1)}(Kr) \tag{13}$$

where $H_0^{(1)}$ is the zeroth-order Hankel function of first kind (or Bessel function of third kind) and $r = \sqrt{x^2 + z^2}$ is the 2D distance from the origin to the point.

Substituting Eq. (13) into the standard Sommerfeld-Rayleigh integral for a limited aperture of size x_0 (in 2D space) [29] and operating, one obtains the new $\varphi_{in}^*(x, z)$:

$$\varphi_{in}^*(x,z) = \frac{1}{4\pi} \int_{-x_0/2}^{x_0/2} U_0(x') \, \frac{iK}{2} \frac{z}{\sqrt{(x'-x)^2 + z^2}} H_1^{(1)} \left[\sqrt{(x'-x)^2 + z^2} \right] dx' \tag{14}$$

where $H_1^{(1)}$ is the first-order Hankel function of first kind and $U_0(x')$ is an adequately chosen incident field. In our case we use $U_0(x') = e^{iK_x x'}$ to simulate a limited aperture wave with arbitrary angle of incidence by setting adequately the value of K_x. Eq. (14) is a common result when one performs the Green's function approximation to a 2D diffraction analysis [29].

The implementation of the algorithm in Section 2.4 is based upon the following approximations:

a) in the right-hand-side of Eq. (5), we replace the incoming plane wave $\varphi_{in}(x, z)$ and the two contributions due to $\mu_1(x)$ and $\mu_2(x)$ by the new $\varphi_{in}(x, z)$ in Eq. (14).
b) in the right-hand-side of Eq. (8) for $i = 3, 4$, we replace the incoming plane wave $\varphi_{in}(x_i')$ and the two contributions due to $\mu_1(x)$ and $\mu_2(x)$ by the new $\varphi_{in}(x_i')$ in Eq. (14). Eq. (8) for $i = 1, 2$ is no longer considered.

Then, Eq. (5) becomes a representation for the slow neutron wavefunction in terms of the new $\varphi_{in}(x, z)$, $\mu_3(z)$ and $\mu_4(z)$. In turn, Eq. (8) for $i = 3, 4$ becomes a new system of two inhomogeneous integral equations for $\mu_3(z)$ and $\mu_4(z)$, with the new inhomogeneous term in Eq. (14).

In Table 1a, we introduce such data (see waveguide data).

3.4.2. Numerical results

Operating as indicated in the previous section we obtain values for $\varphi_{in}(x, z)$, for $\mu_3(z)$ and $\mu_4(z)$. In this case, for an angle of incidence of 20° by adequately setting the value of the component K_x of the wavevector, we had to perform 5 iterations (see Table 1b) to converge to the result. Figs. 5a and 5b show our results. These figures display the squared modulus of the neutron wavefunction, which is represented by means of different colours at each point (x, z).

The results are in good agreement with those expected enhancing the modal structure of the confined neutron beam. Fig. 5a shows that the waveguide exhibits a diffraction pattern because of its aperture. The longer the propagation in the waveguide the more the spatial frequencies mix and then, propagation modes arise. It can be seen in Fig. 5b, where we perform another simulation to zoom a concrete region with more resolution and fine structure is seen.

The computation of Fig. 5b is independent of that of Fig. 5a and took 2195.14 s. In order to obtain Fig. 5b, one must evaluate a new $\varphi_{in}(x, z)$ (since we need to generate those points that were not computed in the first simulation) as well as the total wave, $\varphi(x, z)$ in the counterpart of Eq. (5) for the actual Sommerfeld-Rayleigh approximation. One can make use of the auxiliary functions, $\mu_3(z)$ and $\mu_4(z)$, obtained in the previous calculation.

As computation at each point is independent from those for other points, we focus our attention into particular zones in the simulation. This is our main reason to rely on using numerical integration in step 7, rather that inverse FFT (while the latter implies shorter running times, but higher memory consumption). Any potential user could apply one or another method depending on his/her needs.

Notice that this simulation required about one hour computation in comparison to 80 h for that of Fig. 9 (see subSection 4.1). Apart from this fact, it is interesting to compare the sizes of the apertures in both cases (25 Å versus 10^3 Å) as well as the size of the domain simulated (75 × 2500 Å versus 10^3x10^4 Å).

3.4.3. Iteration procedure: geometrical interpretation

At this point, we represent the wavefunction $\varphi(x, z)$ from step 6, after each iteration. This will show the outcome produced by updating the value of the auxiliary functions $\mu_3(x_0/2, x)$ and $\mu_4(-x_0/2, z)$. Results are shown in Figs. 6a to 6e. These figures display the squared modulus of the neutron wavefunction, which is represented by means of different colours at each point (x, z).

Here we recall the interpretation of the successive iterations of Green's functions in Eq. (2) and (3) discussed by Balian and Bloch. In their work they stated: *"It may be described as a multiple reflection expansion…"* [21]. In our case, each iteration updates the information in $\mu_3(z)$ and $\mu_4(z)$ with the internal reflection produced by the beam in the opposite wall. Notice that it is very similar to the behaviour expected in classical optics, but in the present ranges of distances, diffraction effects are observable and increase with propagation.

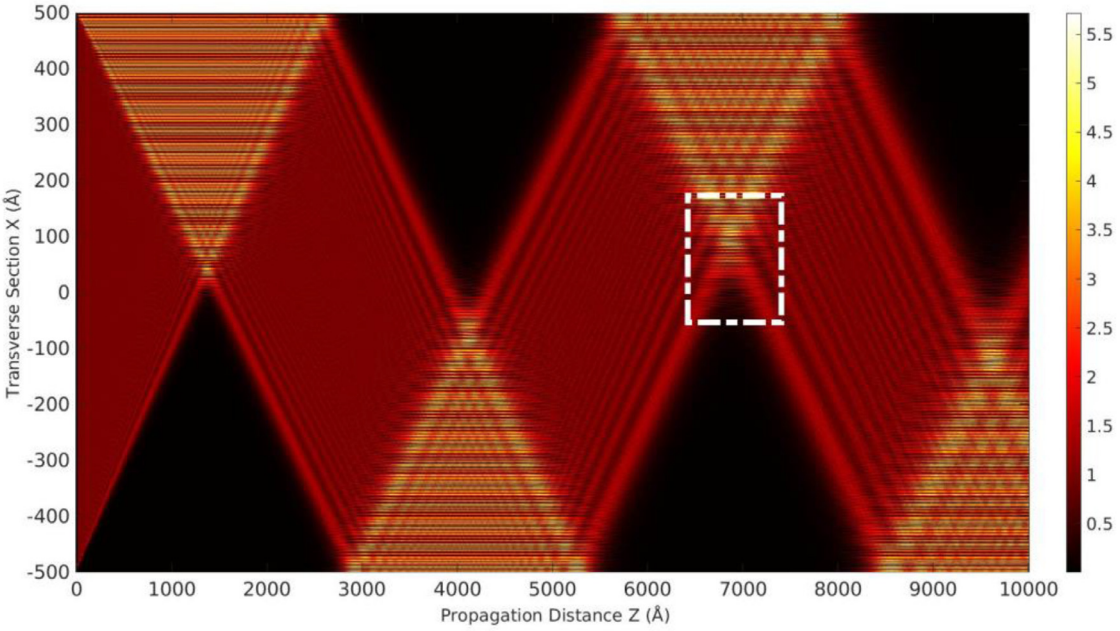

a) Full waveguide.

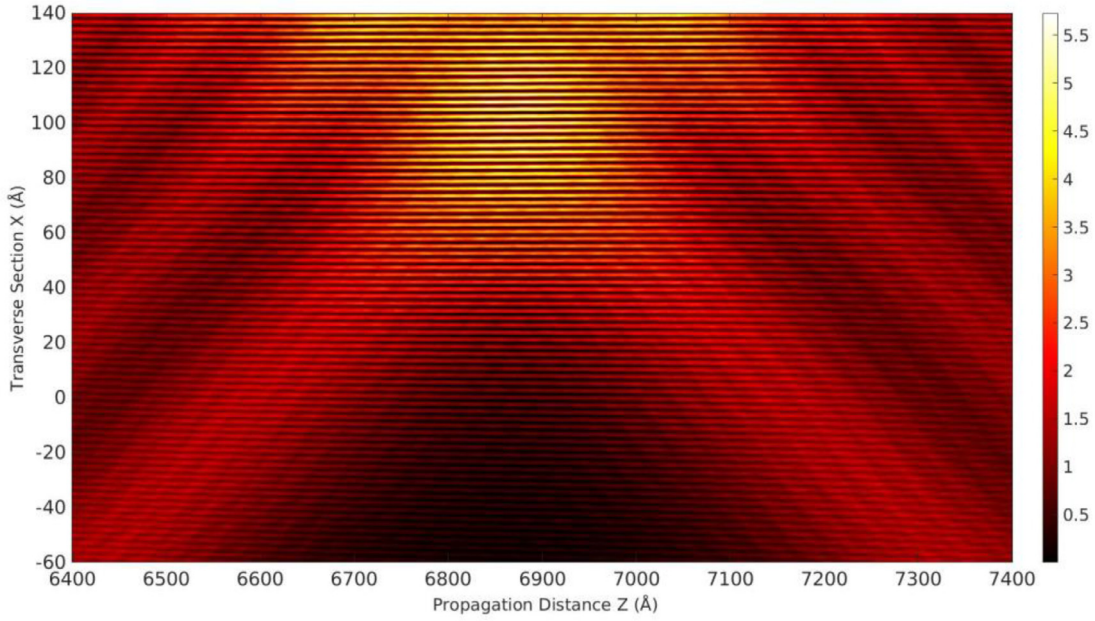

b) Detailed simulation of a zone (white rectangle).

Fig. 5. Propagation of a confined neutron wave (using the Sommerfeld-Rayleigh approximation for simulating the incoming wave) with angle of incidence 20° and $E = 0.025\ eV$ ($\lambda_{db} = 1.8$ Å) in a waveguide of aperture of 1000 Å. a) Full waveguide. b) Detailed simulation of a zone (white rectangle).

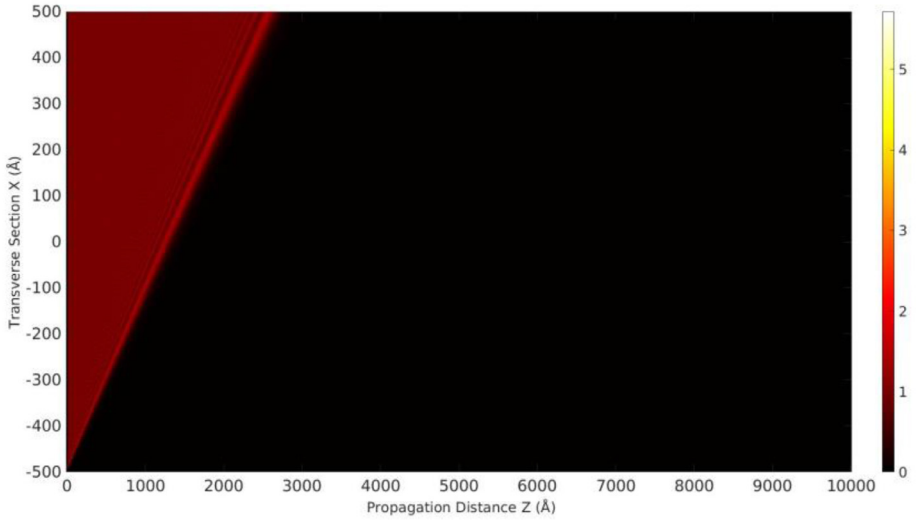

a) Incoming wave, $\varphi_{in}(x, z)$.

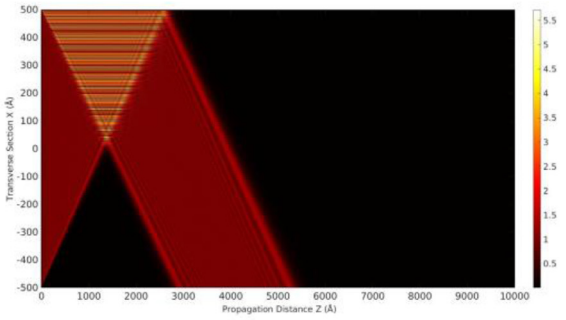

b) One iteration

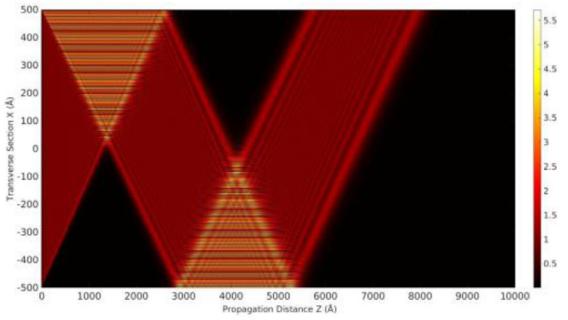

c) Two iterations

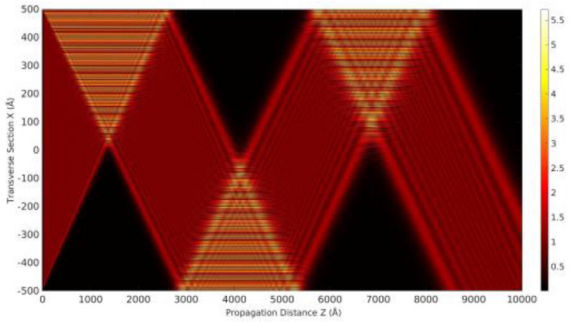

d) Three iterations

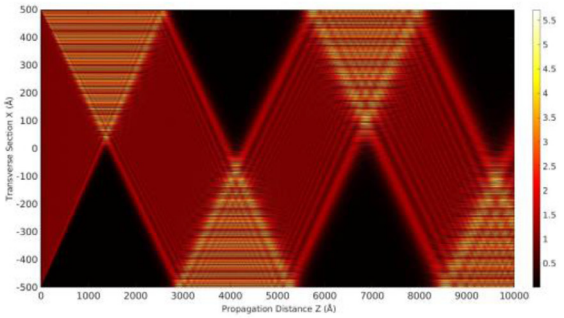

d) Four iterations

Fig. 6. Simulation of iterations: geometrical effect. Angle of incidence 20° and = 0.025 eV (λ_{db} = 1.8 Å). Simulations were made applying numerical integration. a) Incoming wave, $\varphi_{in}(x, z)$. b) One iteration. c) Two iterations. d) Three iterations. d) Four iterations.

3.4.4. Multimedia support for the simulations

In order to display further detailed results, we present a video simulating the behaviour of a neutron wave of energy $E = 0.025\ eV$ for different angles of incidence: $-25° \leq \theta \leq 25$. The video, as previous figures, displays the squared modulus of the neutron wavefunction by means of different colours at each point (x, z).

In this case, our only choice was to make use of inverse FFT algorithm for calculating each frame since, otherwise, the computations would have been extremely time consuming. In this case, the total running time needed to create the video was 1752.71 s (approximately half an hour) for a total of 121 frames.

This video shows that the waveguide with Dirichlet conditions yields a well-defined geometrical propagation modulated by the aperture diffraction. It tends to mix the spatial frequencies as the confined beam propagates. For angles close to 0°, the video shows the formation of interference patterns in sizes that are comparable to the transverse section of the guide. For larger angles, the video shows the presence of spurious Moiré effects, as an artefact, in the triangles formed by the superposition of both incident and outgoing waves with each of the walls (say, the clad). Moire arises because the video resolution grid does not match the spatial frequency of the interaction. This effect could be corrected by increasing the simulation resolution up to an unaffordable cost.

3.5. Case: Fresnel regime for slow neutron beam near field free propagation

In physical optics, different approximations are well established to analyse or solve analytically the diffraction pattern created by an aperture in different regimes under a scalar treatment. One of those approximations is the Fresnel diffraction regime (i.e., near field diffraction). This regime is applicable, in terms of the so-called Fresnel number: $F = a^2/z\lambda$. $F < 1$ corresponds to near field approximation, while $F>1$ corresponds to far field approximation. Here a is the dimension of the object (radius, for example), z is the propagation distance and λ is the wavelength.

In this case, we performed for convenience a 3D simulation of a circular aperture of radius, $R = 100$ Å.

Notice that this case is an extension to 3D regime of the case proposed in Section 3.3. It is indeed a proof of the validity of our algorithm in 3D space (i.e.: adding the, yet unconsidered, y direction) which enables to compare the runtime required for this regime with actual cases. Moreover, it is expected that with the assumption of a circular geometry (in the aperture) the simulation will exhibit focusing effects as a property of Fresnel free propagation of diffracted waves.

Since propagation distance in Fresnel regime holds for $z \approx 5500$ Å the present case requires a high amount of computation to propagate this long distance in comparison to a 2D case. Recalling Table 1 for case "Fresnel Regime", we simulate this aperture by making use of 2D FFT instead of the one dimensional case. In Table 1b, one can observe that running times in these cases are of the same order as numerical integration in 2D cases.

Extending the algorithm used in Section 3.3, we simulate an incoming plane wave with an angle of incidence of 0°, $\varphi_{in}(x, y, z) = e^{iK_{in}z}$, with $K_{in}^2 = 2mE/\hbar^2$, E being the neutron incoming energy ($E = 0.025\ eV$ for thermal neutrons) The incoming wave travels from $z \to -\infty$ and impinges a barrier, where we impose Dirichlet conditions, with a circular aperture of radius, $R = 100$ Å. Thus, Eq. (5) becomes, in this case:

$$\varphi(x, y, z) = \varphi_{in}(x, y, z) - \iint_{-\infty}^{\infty} \frac{\partial G\big(x - x', y - y', z\big)}{\partial z} \mu\big(x', y'\big) dx' dy' \tag{15}$$

Notice that, compared to previous sections, $\mu(x', y')$ is a 2D auxiliary function.

The integration is performed over the whole screen (x', y') for $z = 0$, except over the aperture. As we stated in Section 3.3, the total field, equivalent for this case, will be $\varphi(x, y, z) = \varphi_{in}(x,y, z) + \varphi_{out}(x,y, z)$ where $\varphi_{out}(x,y, z)$ is the wavefunction generated by imposing Dirichlet conditions in the barrier, yielding the auxiliary function for $x^2 + y^2 \geq R^2$ (Notice that in the aperture $\mu(x, y) = 0$).

$\varphi_{out}(x,y, z)$ will cancel (extinguish) $\varphi_{in}(x,y, z)$ in the whole barrier except for those points where $x^2 + y^2 \leq R^2$ (i.e.: the aperture) and, then, propagates as a diffracted wave. The 3D counterpart of the 2D Eq. (8) for the actual auxiliary function for Eq. (15) reads, for $x^2 + y^2 \geq R^2$:

$$\frac{m}{\hbar^2} \mu(x, y) = -\varphi_{in}(x, y, 0) \tag{16}$$

In this case, as in Section 3.3, we only require one iteration since the outgoing wave does not interact again with the barrier (see Table 1b).

Figs. 7a, to 7c show our results displaying the squared modulus of the neutron wavefunction, which is represented by means of different colours at each simulated point.

Figs. 7a to 7c demonstrate that the algorithm simulates correctly the neutron beam focusing as a result of its behaviour as a wave. This result has been experimentally demonstrated by the use of Fresnel zone plates [15].

Moreover, a pattern of minima and maxima in the system axis is shown in Fig. 7a. These structures, called doughnut-like (for the minima), have already been analysed in the context of Fourier diffraction, see for example [30].

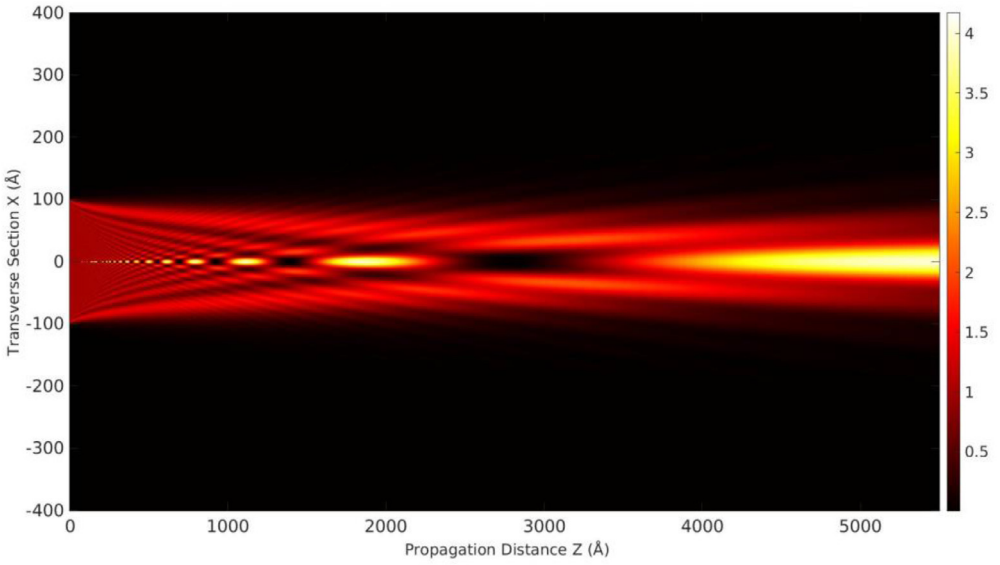

a) Propagation field under Fresnel approximation

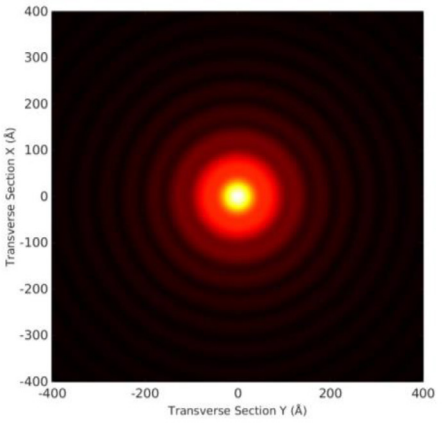

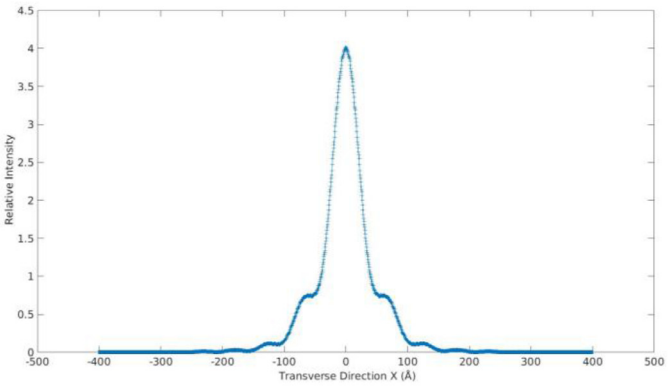

b) Fresnel diffraction at $F \sim 1$ c) Intensity profile at $F \sim 1$

Fig. 7. Simulation of aperture diffraction. Angle of incidence 0° and = 0.025 eV (λ_{db} = 1.8 Å). Simulations were made applying 2D inverse Fast Fourier Transform. a) Propagation field under Fresnel approximation. b) Fresnel diffraction at $F \sim 1$. c) Intensity profile at $F \sim 1$.

3.6. Case: Arago-Poisson spot

Recalling the previous Section 3.5, we have carried out a simulation for determining the arising of the Arago-Poisson spot. This is a particular phenomenon in the shadow of a Fresnel diffraction pattern. It will serve as a proof of the consistency of the proposed simulation method.

By inspecting Section 3.5 and Table 1, it is clear that the mathematical conditions are the opposite of those used in Section 3.5. In the present case, we simulate an incoming plane wave with an angle of incidence of 0°, $\varphi_{in}(x, y, z) = e^{iK_{in}z}$, with $K_{in}^2 = 2mE/\hbar^2$, E being the neutron incoming energy ($E = 0.025\ eV$ for thermal neutrons), travelling from $z \to -\infty$ and impinging a circular plate (instead of a barrier) of radius, $R = 100$ Å.

In the present case, the 3D Dirichlet condition follows the procedure applied to Eq. (15) (yielding Eq. (16)). Contrary to the previous section, 3.5, the auxiliary function reads: $m/\hbar^2 \mu(x, y) = -\varphi_{in}(x, y, 0)$ for $x^2 + y^2 \leq R^2$ and $\mu(x, y) = 0$ elsewhere.

We emphasize that, as in the previous subsection, all calculations are performed in 3D and that one starts out of the actual counterpart of Eq. (15), with the corresponding integration domain ($x^2 + y^2 \leq R^2$).

Fig. 8a shows the squared modulus of the neutron wavefunction by means of different colours at each point (x, z) in the plane $y = 0$. As expected, an on-axis intensity appears in the centre of the shadow of the plate (Arago-Poisson spot). Fig. 8b shows the behaviour of relative intensity (i.e. the squared modulus of the field divided by the squared modulus of φ_{in}) in the axis of the system, as a function of the propagation distance, z, in units of the disc radius R.

The on-axis relative intensity tends to the incoming wave relative intensity, as it would be expected. Moreover, Fig. 8b, shows that Arago-Poisson spot appears just over a few times the plate size, as well expected.

4. Discussion

In subSection 4.1 we discuss the computational cost of the algorithm for previous simulated cases and compare them with previous FDM results. In subSection 4.2 we set a brief discussion about the relationship between spatial frequencies resolution, memory load and propagation distance. In subSection 4.3, we state our main conclusions and possible applications of this algorithm.

4.1. Computation time and memory load

All our simulations where performed in a personal computer laptop MSI Intel Core i5 (7th gen) with 8GB-DDR4 RAM memory, under software MATLAB-2020a running on Linux Ubuntu18.04. Fast Fourier Transform (FFT) and Inverse Fast Fourier Transform (IFFT) libraries used are those included in MATLAB software. This computer has 4 CPU as well as a Nvidia GeForce 1050 GTX graphics card. Nevertheless, we have not implemented code parallelization or CUDA computing, so all running times come from one single CPU.

Table 1a summarizes the performance results in memory consumption while Table 1b does on computation time.

In a previous paper [18] we explored numerically the possibility of slow neutron confinement in 2D waveguides. For that purpose, we simulated, using Finite Difference Time Domain (FDTD) algorithm directly applied to the Schrödinger equation (see [17] and references therein), the behaviour of a thermal neutron plane wave striking an aperture of 25 Å and its diffraction pattern propagated on air. We compared them with the one for the propagation mode for a Hg-Ti-Hg thin layer (chosen for maximizing the confinement effect). Fig. 9 displays the results of numerical simulations for a propagation mode. The figure represents the gain in the Hg-Ti arrangement in comparison with air propagation in percentage, according to the formula:

$$Gain = \frac{\left(\varphi_{Hg-Ti}(x,z) - \varphi_{air}(x,z)\right)^2}{\varphi_{air}(x,z)^2}\% \tag{17}$$

That simulation (since Dirichlet boundary conditions were not imposed) demonstrates the computational challenges and limitations that one may face (taking into account the relationships between the system's aperture, propagation... versus the beam wavelength).

In order to obtain those results, the cost was about 80 h of computation in a personal laptop and led to deal with various matrices of 1 GB average memory: the results display the limitations of that method. If one would try to apply it to larger scales (i.e., a wider transverse section of the guide or longer propagation distances, as needed) the computing cost would be extremely high.

Comparing these computation times, memory load and propagation distance with results in Table 1a and 1b, the algorithm used in [18] demonstrates to be less efficient by various orders of magnitude.

4.2. Resolution vs propagation

The implementation of our algorithm may be linked to signal theory as follows. For a given input signal (the incident wave, $\varphi_{in}(x,z)$), the algorithm calculates, as the boundary is approached, each of the auxiliary functions, $\mu_i(x, z)$, and then it propagates them, iteratively, and performs the decomposition into spatial frequencies. Once convergence is achieved, the output signal (i.e.: $\varphi(x, z)$) solves the problem for this particular geometry with Dirichlet boundary conditions.

Since the algorithm is based upon performing the spectral analysis of the input signal, it is critical to have an adequate control of where are the high cutoff frequencies. It is intuitive that longer simulation time and higher resolution in spatial frequencies will require a higher number of points to compute (i.e. higher memory load and running time).

In our case, since we use MATLAB FFT libraries to perform our computations, an input array of N_p complex numbers, $\{x_n\} := x_0, x_1, \ldots, x_{N_p-1}$ yields a discrete Fourier transform of N_p points with spatial frequencies defined in the range: $K \in [-N_p/2, (N_p/2) - 1]$, for N_p an even number and $K \in [-(N_p - 1)/2, (N_p - 1)/2]$ for an N_p odd number.

In our code, our main parameter to be controlled is the highest spatial frequency, K_{max}, that corresponds to the value $N_p/2 - 1$. Since we simulate a waveguide, this parameter must be chosen to be larger than the incoming neutron wavevector: $K_{max} > K_{in} = \sqrt{2mE/\hbar^2}$. This allows all possible propagation modes to be computed. Nevertheless, this K_{max} must be carefully chosen since the integration over those modes with $K > K_{in}$ will give rise to evanescent modes that can be neglected in our set up.

On the other hand, one must correlate the array of complex numbers $\{x_n\}$ with the different spatial points, (x, z).

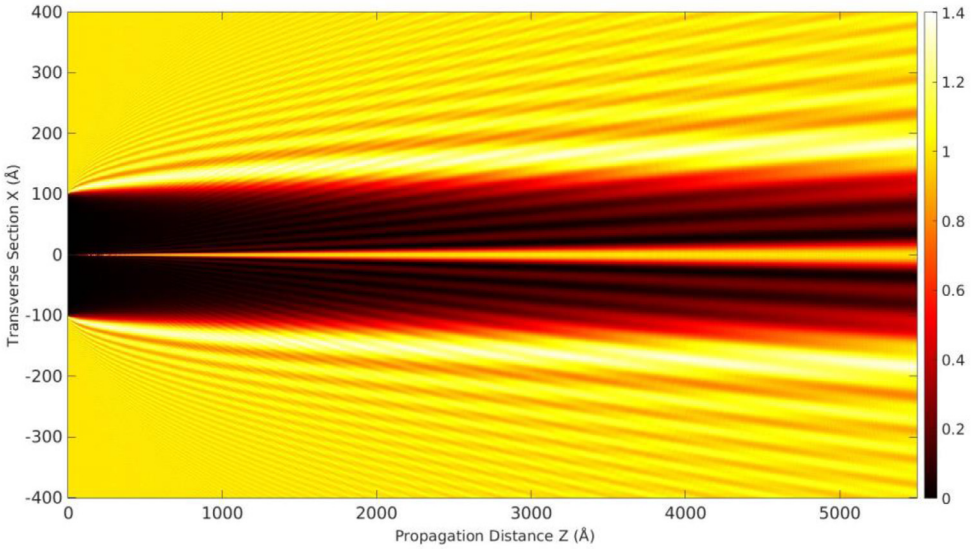

a) Propagation field in the Fresnel regime of a slow neutron beam, exhibiting the formation of the Arago-Poisson spot at the center of the shadow region

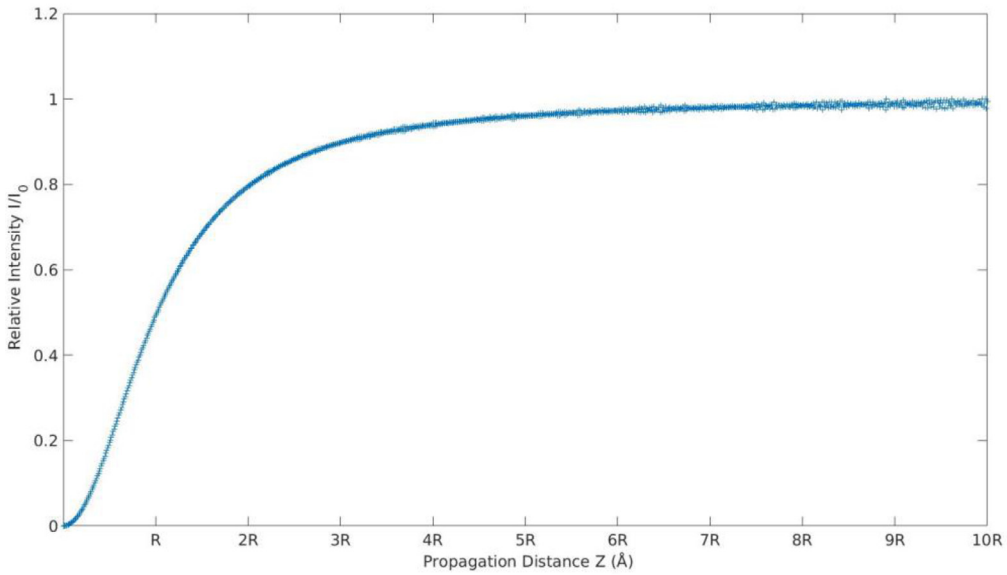

b) Relative intensity versus disc radius R for free propagation

Fig. 8. Simulation of circular plate diffraction. Angle of incidence 0° and $= 0.025\ eV$ ($\lambda_{db} = 1.8$ Å). Simulations were made applying 2D inverse Fast Fourier Transform. a) Propagation field in the Fresnel regime of a slow neutron beam, exhibiting the formation of the Arago-Poisson spot at the centre of the shadow region. b) Relative intensity versus disc radius R for free propagation.

Table 1a
Memory requirements for computing each case, comparing numerical integration versus Inverse Fast Fourier Transform.

Case	Method	Auxiliary Functions μ_i required and points of deffinition	Matrix Size (NxM) Complex double precision	Matrix Size (Megabytes)
15 º Reflection	Numerical Integration	$\mu_1(x)$ at $z=0$	3 matrices 1001x5001	3 matrices 80 MB
	Inverse FFT	$\mu_1(x)$ at $z=0$	3 matrices 1001x16384	3 matrices 262 MB
30 º Reflection	Numerical Integration	$\mu_1(x)$ at $z=0$	3 matrices 1001x5001	3 matrices 80 MB
	Inverse FFT	$\mu_1(x)$ at $z=0$	3 matrices 1001x16384	3 matrices 262 MB
0º Aperture Diffraction	Numerical Integration	$\left.\begin{matrix}\mu_1\left(x\geq\frac{x_0}{2}\right)\\ \mu_2\left(x\leq-\frac{x_0}{2}\right)\end{matrix}\right\}at\ z=0$	1 matrix 1001x5001	1 matrix 80 MB
	Inverse FFT	$\left.\begin{matrix}\mu_1\left(x\geq\frac{x_0}{2}\right)\\ \mu_2\left(x\leq-\frac{x_0}{2}\right)\end{matrix}\right\}at\ z=0$	1 matrix 1001x16384	1 matrix 262 MB
10 º Aperture Diffraction	Numerical Integration	$\left.\begin{matrix}\mu_1\left(x\geq\frac{x_0}{2}\right)\\ \mu_2\left(x\leq-\frac{x_0}{2}\right)\end{matrix}\right\}at\ z=0$	1 matrix 1001x5001	1 matrix 80 MB
	Inverse FFT	$\left.\begin{matrix}\mu_1\left(x\geq\frac{x_0}{2}\right)\\ \mu_2\left(x\leq-\frac{x_0}{2}\right)\end{matrix}\right\}at\ z=0$	1 matrix 1001x16384	1 matrix 262 MB
Waveguide	Numerical Integration	Sommerfel-Rayleigh approximation (see 3.4.1) $\mu_3(z\geq 0)atx=\frac{x_0}{2}$ $\mu_4(z\geq 0)atx=\frac{-x_0}{2}$	4 matrices 500x1001 6 matrices 1x32768	4 matrices 8 MB 6 matrices 0.5 MB
	Inverse FFT	$\left.\begin{matrix}\mu_1\left(x\geq\frac{x_0}{2}\right)\\ \mu_2\left(x\leq-\frac{x_0}{2}\right)\end{matrix}\right\}at\ z=0$ $\mu_3(z\geq 0)at\ x=\frac{x_0}{2}$ $\mu_4(z\geq 0)at\ x=\frac{-x_0}{2}$	4 matrices 16384x1592 * 8 matrices 1x32768	4 matrices 412 MB 8 matrices 0.5 MB
Fresnel Regime	2D Inverse FFT**	$\mu_1(x,y)at\ z=0$	6 matrices 4096x4096	6 matrices 264 MB
Poisson Spot	2D Inverse FFT**	$\mu_1(x,y)at\ z=0$	6 matrices 4096x4096	6 matrices 264 MB

*Note: These matrices were reduced by deleting superfluous information to save memory. Otherwise their size would be 16,384 × 32,768 complex double precision (about 8.6 GB each matrix).
**Note: These simulations were performed in 3D by simulating a circular aperture or plate.

In our case, a direct calculation shows that, once K_{max} is fixed, we deal with values of K, and z in the ranges:

$$K\in\left[\frac{-N_p}{2}\frac{K_{max}}{\frac{N_p}{2}-1},K_{max}\right] \tag{18}$$

$$z\in\left[-2\pi\frac{\frac{N_p}{2}\left(\frac{N_p}{2}-1\right)}{K_{max}(N_p-1)},2\pi\frac{\left(\frac{N_p}{2}-1\right)^2}{K_{max}(N_p-1)}\right] \tag{19}$$

z being the propagation distance along the waveguide. Notice that the same relationship may be established for the transverse coordinate x with a different value of K_{max} (ie, since those coordinates are independent of each other, one may define

Table 1b
Running times data for each case, comparing numerical integration versus Inverse Fast Fourier Transform.

Case	Method	Step 1 Generate φ	Step 2 Calculate μ_i	Steps 3-6 Iterations	Step 7 Final result	TOTAL
15 º Reflection	Numerical Integration	6.00 s	0.08 s	1 iteration 0.40 s	2567.24 s	2573.69 s
	Inverse FFT	109.87 s	0.08 s	1 iteration ~0 s	0.71 s	110.67 s
30 º Reflection	Numerical Integration	3.30 s	0.07 s	1 iteration 0.03 s	2595.72 s	2599.11 s
	Inverse FFT	103.34 s	0.05 s	1 iteration 0.01 s	0.67 s	104.07 s
0º Aperture Diffraction	Numerical Integration	-	0.20 s	1 iteration 0.491 s	2576.75 s	2577.45 s
	Inverse FFT	-	0.19 s	1 iteration 0.01 s	0.71 s	0.90 s
10 º Aperture Diffraction	Numerical Integration	-	0.14 s	1 iteration 0.07 s	2572.84 s	2573.04 s
	Inverse FFT	-	0.22 s	1 iteration ~0 s	0.53 s	0.75 s
Waveguide	Numerical Integration	2D S-R* 1585.22 s	2D S-R* 103.94 s	5 iterations 541.45 s	1030.29 s	3260.91 s
	Inverse FFT	10.27 s	0.01 s	5 iterations 0.07 s	4.03 s	14.39 s
Fresnel Regime	2D Inverse FFT**	-	0.84 s	1 iteration 0.91 s	1276.87 s	1278.62 s
Poisson Spot	2D Inverse FFT**	-	1.65 s	1 iteration 0.48 s	1335.96 s	1338.09 s

*Note: φ_{in} and $\mu_i(x)\, i = 1, 2$ for this case are calculated through numerical integration of the Sommerfeld-Rayleigh integral for 2D Green's function (see Section 3.4.1).
**Note: These simulations were performed in 3D by simulating a circular aperture or plate.

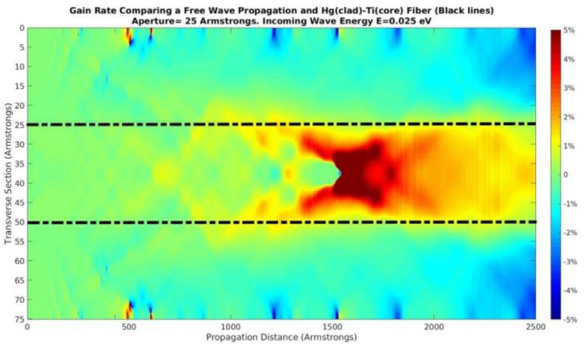

Fig. 9. FDTD simulation comparing a free neutron wave in a 25 Å aperture VS 25 Å aperture Hg-Ti waveguide. Gain in percentage is represented according to Eq. (17). Ti core is represented between black dotted lines. Figure from [18].

different ranges in propagation and spatial frequencies for longitudinal and transversal analysis). Notice as well that the range for K corresponds to an even value of N_p. This is because we always use values of N_p as powers of 2, since FFT algorithm has a better performance with it.

By inspecting Eq. (19), one realizes that the maximum propagation distance achievable and the maximum frequency to analyse are related between them and related, as well, to the number of points simulated. Consequently, for propagating

a neutron beam with a defined wavevector, one may achieve longer distances only by increasing the number of points simulated (as expected).

4.3. Conclusions and future work

In this paper, we have presented a new, efficient and robust method for computing confined neutron beam propagation for those cases in which Dirichlet boundary conditions play a key role. The algorithm (subSection 2.4) is versatile and powerful to deal with: a) reflection (subSection 3.2) for arbitrary angles, b) single–slit diffraction (subSections 3.3, 3.5 and 3.6) for any angle of incidence, c) waveguiding regime (subSection 3.4) and d) free propagation and its relation with Fresnel regime.

The scope of this algorithm, even if developed in the context of neutron optics, goes beyond the neutron wave propagation by means of FFT. The relationships emerging here allow solving the problem in the entire space by performing only computations over the boundaries (thus, reducing one dimension the entire problem). In this case, the possibility of performing these computations using FFT results in an additional improvement.

The potentialities of this algorithm would be useful in any physical field involving wave equations in which geometrical dimensions are several orders of magnitude larger than the wavelength, making hard its computation based upon standard Finite Differences Methods.

The method has plenty of advantages in: a) saving memory, since matrices size is not linked with the wavelength, b) running time, since the code allows direct parallelization and the use of FFT algorithms, and c) the possibility of focusing attention on specific zones or areas of interest. All these features become a great advantage in cases, such as neutron optics, where geometrical parameters are some orders of magnitude larger than wavelengths.

We remark that the method presented here is constrained to simulate the wave equation instead of those more general methods capable of solving different differential equations. Since it is specifically derived to deal with scalar wave equation and strict Dirichlet boundary conditions [1], it does not admit for modifications trying to discuss penetrations of the neutron into a finitely repulsive clad. We performed different attempts for the latter purpose without success, concluding that another entirely different approach would be required. Conversely, one would expect that the reliability of the present algorithm, for strict Dirichlet boundary conditions, would improve if, instead of neutrons, it were applied to more massive particles (say atoms) penetrating much less into the repulsive clad.

While this could be considered a meshless method, the maximum spatial frequency is limited, as discussed in Section 4.2, by the number of points used for computing auxiliary functions, μ_i. Conversely, the simulation of a number of sharp edges (i.e. corners) may lose its fine structure in exchange of improving computation times. Anyway this method is an important improvement compared to those FDM.

Notice that, as exposed in Section 2, this algorithm, as a first step, requires to know explicitly how the incident wave, φ_{in}, impinges the boundaries. In the studied cases, this is trivial, but it could be tricky if one deals with more complex geometries (for instance, one wall shadowing another).

For last, there are potentially interesting cases, lying outside our scope here (subwavelength geometries, bended waveguides…), in which the algorithm has not yet been tested, while the basic equations stated in [1] remain.

We emphasize that the algorithm gives, in each studied case, the wavefunction (a complex number) at each point calculated. A global study of the distribution of those complex numbers over the corresponding 2D spatial domains would require a separate study (involving Fourier transforms), which lies outside our scope here.

We centred our attention both in the most known optical scenarios (in order to establish a proper benchmark for expected results) and on our physical motivation (namely, neutron waveguides). This connection to optics and the well performance of the algorithm could enable to establish a routine procedure to designing neutron waveguides.

One possible next step would be to expand the algorithm to solve more general boundary conditions problems, including those involving different propagation media. In any case, the formulation presented here may be used as a zeroth-order approximation to characterize, for example, other situations for waveguides in which the angle of incidence is lower than the critical angle (total internal reflection). In general, this algorithm is ready to be easily extended for simulating any arbitrary number of surfaces obeying Dirichlet conditions and, more generally, in any problem involving Dirichlet boundary conditions (acoustics, geophysics…).

The propagation of slow neutron waves is not the only case of matter waves that has been experimentally achieved. Apart from neutrons [15], wave-particle duality has been experimentally demonstrated for neutral atoms, such as He [31], deuterium molecule (D_2) [32] and even for C_{60} [33]. Some of these experiments involve the use of optical devices such as Fresnel zone plates and diffraction gratings. The particle behaviour in these experiments may be properly simulated, at least as a zeroth-order approximation, by using this algorithm.

To end, our algorithm may be used in digital holography, since one may simulate, also as a zeroth-order approximation, the interaction of a plane wave beam with a surface with arbitrary shape (through the Dirichlet condition): the reflection of the waves in the surface and their interference with the incoming plane wave may be used to calculate the interference pattern that would appear in any arbitrary point in space. For a previous study, entirely unrelated to the present study and algorithm, see [34]. A convenient reading system of that pattern would eventually lead to the reconstruction of the hologram. In this scenario, the main advantage of the present algorithm would be: a) a correct simulation of the interference

pattern for objects with sizes much larger than the wavelength, at an affordable computational cost, and b) the possibility of focusing in obtaining only the interference pattern.

Funding

We acknowledge financial support from Universidad Complutense de Madrid (FECI-EU-17–06) and Ministry of Science and Innovation (Project PGC2018–094684-B-C21), Spain.

Declaration of Competing Interest

None.

Acknowledgements

We are grateful to Mr David Fernández for kind help.

Supplementary materials

Supplementary material associated with this article can be found, in the online version, at doi:10.1016/j.apm.2021.09.007.

References

[1] I. Molina de la Peña, M.L. Calvo, R.F. Álvarez-Estrada, Neutron waveguides in neutron optics: Green's functions formalism with Dirichlet boundary conditions, J. Mod. Opt. 67 (10) (2020) 899–913, doi:10.1080/09500340.2020.1786181.
[2] G.E. Bacon, Neutron Diffraction (2nd Ed.), Monographs on the Physics and Chemistry of Materials, Oxford University Press, London, 1962, doi:10.1016/0029-5582(62)91045-3.
[3] R.F. Alvarez-Estrada, M.L. Calvo, Chapter 1: Neutron Optics: Fundamentals, in: M.L. Calvo, R.F. Alvarez-Estrada (Eds.), Advances in Neutron Optics: Fundamentals and Applications in Materials Science and Biomedicine, CRC Press, Boca Raton (FL, 2019, pp. 3–78, doi:10.1201/9780367816056.
[4] R.E. De Wames, S.K. Sinha, Possibility of guided-neutron-wave propagation in thin films, Phys. Rev. B. 7 (3) (1973) 917–921, doi:10.1103/PhysRevB.7.917.
[5] R.F. Alvarez-Estrada, M.L. Calvo, Neutron fibres: a possible application of neutron optics, J. Phys. D: Appl. Phys. 17 (3) (1984) 475–502, doi:10.1088/0022-3727/17/3/007.
[6] M.L. Calvo, R.F. Alvarez-Estrada, Neutron fibres (II): some improving alternatives and analysis of bending losses, J. Phys. D: Appl. Phys. 19 (6) (1986) 957–973, doi:10.1088/0022-3727/19/6/012.
[7] Y.P. Feng, C.F. Majkrzak, S.K. Sinha, et al., Direct observation of neutron-guided waves in a thin-film waveguide, Phys. Rev. B. 49 (15) (1994) 10814–10817, doi:10.1103/PhysRevB.49.10814.
[8] S.P. Pogossian, A.Le Menelle, H. Gall, et al., Experimental observation of guided polarized neutrons in magnetic-thin-film waveguides, Phys. Rev. B. 53 (21) (1996) 14359–14363, doi:10.1103/PhysRevB.53.14359.
[9] A. Menelle, S.P. Pogossian, H. Le Gall, et al., Observation of magnetic films neutron waveguides, Phys. B. 234 (1997) 510–512, doi:10.1016/S0921-4526(96)01028-9.
[10] S.P. Pogossian, A. Le Menelle, H. Gall, et al., Observation of neutron guided waves from the open end of a thin film waveguide and a waveguide interferometry, J. Appl. Phys. 83 (3) (1997) 1159–1162, doi:10.1063/1.366810.
[11] S.P. Pogossian, Enhanced neutron concentration in uranium thin film waveguides, J. Appl. Phys 102 (10) (2007) 104501, doi:10.1063/1.2811851.
[12] S.V. Kozhevnikov, Y.N. Khaydukov, T. Keller, et al., Polarized neutron channeling as a tool for the investigations of weakly magnetic thin films, JETP Lett 103 (1) (2016) 36–40, doi:10.1134/S002136401601008.
[13] M.A. Kumakhov, V.A. Sharov, A neutron lens, Nat. 357 (6377) (1992) 390–391, doi:10.1038/357390a0.
[14] H. Chen, G. Downing, D.F.R. Mildner, et al., Guiding and focusing neutron beams using capillary optics, Nat. 357 (6377) (1992) 391–393, doi:10.1038/357391a0.
[15] P. Kearney, A. Klein, G. Opat, et al., Imaging and focusing of neutrons by a zone plate, Nat. 287 (5780) (1980) 313–314, doi:10.1038/287313a0.
[16] K.S. Yee, Numerical solution of initial boundary value problems involving Maxwell's equations in isotropic media, IEEE Trans. Antennas Propagat. A14 (3) (1966) 302–307, doi:10.1109/TAP.1966.1138693.
[17] J.R. Nagel, A review and application of the finite-difference time-domain algorithm applied to the schrödinger equation, Aces J 24 (1) (2009) 1–8.
[18] R.F. Alvarez-Estrada, I. Molina de la Peña, M.L. Calvo, Focalizing slow neutron beams at and below micron scales: discussion on BNCT. Phosphorus, Sulfur Silicon Relat Elems. 193 (2) (2018) 64–73, doi:10.1080/10426507.2017.1417300.
[19] A. Shojaei, Galvanetto, T.U. Rabczuk, A., F. Jenabi, M. Zaccariotto, A generalized finite difference method based on the peridynamic differential operator for the solution of problems in bounded and unbounded domains, Comput. Methods. Appl. Mech. Engrg. 343 (2018) 100–126, doi:10.1016/j.cma.2018.08.033.
[20] A. Shojaei, F. Mossaiby, M. Zaccariotto, U. Galvanetto, A local collocation method to construct Dirichlet-type absorbing boundary conditions for transient scalar wave propagation problems, Comput. Methods. Appl. Mech. Engrg. 356 (2019) 629–651, doi:10.1016/j.cma.2019.07.033.
[21] R. Balian, C. Bloch, Distribution of eigenfrequencies for the wave equation in a finite domain: I. Three-dimensional problem with smooth boundary surface, Ann. Phys. (N.Y.). 60 (2) (1970) 401–447, doi:10.1016/0003-4916(70)90497-5.
[22] M. Nieto-Vesperinas, Propagación de luz y otras ondas electromagnéticas: difracción y esparcimiento [Light and electromagnetic waves propagation: scattering and diffraction], in: M.L. Calvo (Ed.), Óptica Avanzada [Advanced Optics], Ariel Ciencias, Barcelona, Spanish, 2002, pp. 41–82.
[23] M. Nieto-Vesperinas, Scattering and Diffraction in Physical Optics, Wiley-Interscience, New York (NY), 1991.
[24] L. Mandel, E. Wolf, Optical Coherence and Quantum Optics, Cambridge University Press, Cambridge, 1995, doi:10.1017/CBO9781139644105.
[25] O.D. Kellogg, in: Foundations of Potential Theory, Springer-Verlag, Berlin-Heidelberg-New York, 1967, pp. 175–211, doi:10.1007/978-3-642-86748-4.
[26] J.W. Cooley, J.W. Turkey, An algorithm for the machine calculation of complex Fourier series, Math. Comp. 19 (90) (1965) 297–301, doi:10.2307/2003354.
[27] M. Frigo, S.G. Johnson, The design and Implementation of FFTW3, Proc. IEEE 93 (2) (2005) 216–231, doi:10.1109/JPROC.2004.840301.
[28] J. Schwinger, L. Deraad Jr, K. Milton, W.Y. Tsai, Classical Electrodynamics, CRC Press, Boca Raton, 1998, doi:10.1201/9780429503542.
[29] M.L. Calvo, Linear behaviour in the aperture pupil of single photoreceptors: consequences related to the degree of inhomogeneity, Biol. Cybern. 54 (3) (1986) 201–210, doi:10.1007/BF00356859.
[30] J. Ojeda-Castaneda, C. Gomez-Reino, Selected Papers on Zone Plates, SPIE Press, Washington, 1996.
[31] O. Carnal, M. Sigel, T. Sleator, H. Takuma, J. Mlynek, Imaging and focusing of atoms by a Fresnel zone plate, Phys. Rev. Lett. 67 (23) (1991) 3231–3234, doi:10.1103/PhysRevLett.67.3231.

[32] T. Reisinger, B. Holst, Neutral atom and molecule focusing using a Fresnel zone plate, J. Vac. Sci.Technol. B 26 (6) (2008) 2374–2379, doi:10.1116/1.2987955.
[33] M. Arndt, O. Nairz, J. Vos-Andreae, C. Keller, G. van der Zouw, A. Zeilinger, Wave-particle duality of C-60 molecules, Nat. 401 (6754) (1999) 680–682, doi:10.1038/44348.
[34] R.F. Alvarez-Estrada, Quantum diffractive reflection for a periodic non-penetrable surface: a multiple scattering approach, Ann. Phys. 204 (1) (1990) 124–154, doi:10.1016/0003-4916(90)90123-6.